

**Crystal structures, binding interactions, and ADME evaluation of brain penetrant
N-substituted indazole-5-carboxamides as subnanomolar, selective monoamine
oxidase B and dual MAO-A/B inhibitors**

Nikolay T. Tzvetkov ^{a,*}, Hans-Georg Stammer ^b, Beate Neumann ^b, Silvia Hristova ^c,

Liudmil Antonov ^c, Marcus Gastreich ^d

^a *NTZ Lab Ltd., Krasno selo 198, Sofia 1618, Bulgaria*

^b *Department of Chemistry, University of Bielefeld, Universitätsstr. 25, 33615 Bielefeld, Germany*

^c *Bulgarian Academy of Sciences, Institute of Organic Chemistry, Centre of Phytochemistry, Acad. G. Bonchev Str., Bl. 9, Sofia 1113, Bulgaria*

^d *BioSolveIT GmbH, An der Ziegelei 79, 53757 St. Augustin, Germany*

KEYWORDS:

ADME; MAO inhibitors; Molecular modeling; Indazole-5-carboxamides; Parkinson's disease; X-ray

* Corresponding author.

E-mail address: ntzvetkov@ntzlab.com (N. T. Tzvetkov). *Phone:* +49-179-528-4358

Abstract

The pharmacological and physicochemical analysis of structurally optimized *N*-alkyl-substituted indazole-5-carboxamides, developed as potential drug and radioligand candidates for the treatment and diagnosis of Parkinson's disease (PD) and other neurological disorders, is reported. Recent efforts have been focused on the development of subnanomolar potent, selective MAO-B (N1-alkyl-substituted compounds **12a–14a** and **15**) and dual active MAO-A/B (N2-methylated compounds **12b–14b**) inhibitors with nanomolar potency towards MAO-B and moderately active against MAO-A enzyme, respectively. The most promising drug-like derivatives in both series were *N*-(3-chloro-4-fluorophenyl)-1-methyl-1*H*-indazole-5-carboxamide (**13a**, NTZ-1441, IC₅₀ hMAO-B 0.662 nM, >15000-fold selective versus MAO-A) and *N*-(3-chloro-4-fluorophenyl)-2-methyl-2*H*-indazole-5-carboxamide (**13b**, NTZ-1442, IC₅₀ hMAO-B 8.08 nM, IC₅₀ hMAO-A 0.56 μM, SI = 70). Moreover, compounds **13a** and **13b** were predicted to cross both the gastrointestinal tract (at pH 2.0, 5.5, and 7.4) and the blood-brain barrier (BBB) *in vitro* with appropriate drug-like properties required for CNS active drugs. Combined single X-ray/molecular modeling studies provided insights into the enzyme–inhibitor interactions within both MAO isoforms and the rationale for their inhibitory activity with controlled MAO-A/B selectivity – despite their small structural differences. The binding modes of **12a,b** and **13a,b** confirmed that the major interactions with hMAO-B were established via the flexible carbonyl group of the carboxamide linkage and the electron-donating nitrogens N1 or N2 of the indazole moiety, allowing further exploration of the alkyl side chain for next step lead optimization efforts.

1. Introduction

Parkinson's disease (PD) is the second most prevalent chronic neurodegenerative disorder of the central nervous system (CNS), typically characterized by the deficiency of the neurotransmitter dopamine (DA) in the nigrostriatal pathway. It results in a progressive impairment of the core motor functions and can be recognized by the major symptoms of bradykinesia (slowness), rigidity, resting tremor, and postural instability, as well as by various non-motor symptoms such as depression, behavioral and cognitive complications that are using to clinical diagnose of PD [1–4]. To date, drugs approved for the treatment of PD are those acting on the dopaminergic and monoaminergic systems [5–7]. In particular, a combination of levodopa replacement therapy with DA agonists, DOPA-decarboxylase inhibitors (DDIs), as well as monoamine oxidase B (MAO-B) and/or catechol-*O*-methyltransferase (COMT) inhibitors are often used for the treatment of PD [1,3,8]. Most of the currently approved medicines have an impact of several motor symptoms especially in early-stage PD, but do not replace the loss of neuronal cells or stop the disease progression [9,10].

Monoamine oxidases (MAOs, EC 1.4.3.4) are mitochondrial flavoenzymes that are involved in the oxidative deamination of exogenous and endogenous amines, including neurotransmitters in both the peripheral nervous system (PNS) and CNS. Two subtypes of MAOs have been identified in mammals, MAO-A and MAO-B, encoded by distinct genes with opposite orientation on the X-chromosome (Xp11.23-11.4), where they share ~70% identity of the protein sequence [11,12]. Both MAO isoforms are essential for the inactivation of monoaminergic neurotransmitters but display regional differences in enzyme activity, substrate preference and distribution in the human brain, and therefore, different clinical significances [13,14]. For example, DA is a substrate for both isoforms but it is mainly metabolized by MAO-B in the *substantia nigra*, where MAO-B is the main form in glial cells and the increased MAO-B activity may lead to dopamine deficiency in the human brain, whereas serotonin (5-hydroxytryptamine, 5-HT) is preferentially degraded by MAO-A and the loss of MAO-A in humans is associated with aggressive behavior [13]. The expression levels and activity of MAO-B in the human

brain, rather than those of MAO-A, increase ~4-fold with aging, leading to a higher production of hydrogen peroxide (H₂O₂) and other reactive oxygen species (ROS), which are associated with oxidative stress and neuronal cell death [15,16]. Enhanced activity and overexpression of MAO-B in the brain is thus observed in patients with Alzheimer's disease (AD) and PD [14,17,18]. Due to their affinity for specific neurotransmitters, selective inhibition of MAO enzymes is an established approach for treating mental disorders (MAO-A) and PD (MAO-B) [19–26].

For example, selective MAO-A inhibitors such as the irreversible inhibitor clorgyline and the reversible inhibitor moclobemide are used in the treatment of depression and anxiety (for structures, see Fig. 1) [19,20]. The irreversible MAO-B inhibitors selegiline and rasagiline are currently applied in PD monotherapy or in a combination with levodopa in late-stage PD [21,22]. However, irreversible MAO inhibition may cause pharmacological side effects and safety complications [23]. Recently, safinamide has been approved as an add-on drug to DA agonists or to levodopa for the treatment of motor symptoms in patients with early or mid-to late-stage PD [24,25]. Safinamide is a multitarget compound exhibiting both, dopaminergic properties (selective and reversible inhibition of MAO-B and DA reuptake) and non-dopaminergic mechanism of action, including selective sodium channel blockade and calcium channel modulation with consequent inhibition of the excessive glutamate release [26].

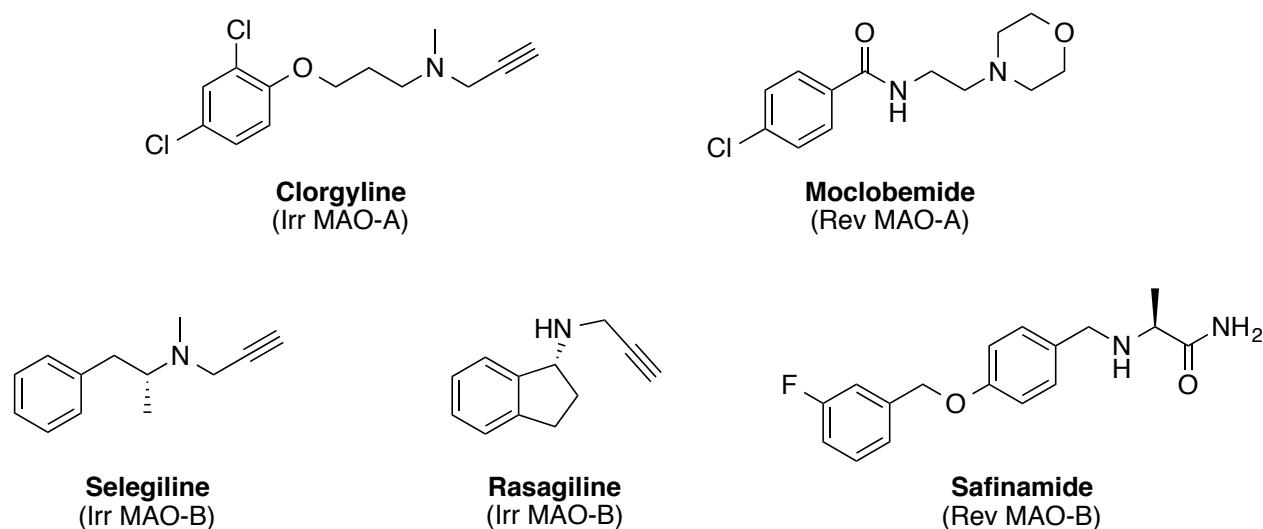


Fig. 1. Structures of irreversible (Irr) and reversible (Rev) MAO inhibitors in clinical use.

Considering the beneficial role of reversible MAO inhibition in neuroprotection and modulation of various pathophysiological processes associated with PD [27], dual and reversible inhibitors of MAO A and B, rather than single MAO-B inhibitors, may have increased therapeutic and neuroprotective potential not only in the treatment of PD but also for AD therapy. Such compounds should inhibit MAOs selectively in the brain with slight preference for MAO-B than for the A-form compared to the inhibition of these enzymes in the peripheral tissues [28]. Moreover, it has been observed that brain-selective MAO drugs may exhibit the combined benefit of antioxidative and neurorestorative activities with a reduced risk for toxicity and side effects [29].

Because of the promising pharmacological properties and favorable safety profiles associated with reversible MAO inhibitors (MAOIs), we have been particularly interested in developing such inhibitors. Recently we have reported the discovery of a series of novel selective, reversible and competitive MAO-B inhibitors with subnanomolar potency [30,31]. Applying a structure-based drug design strategy, we performed systematic structural modifications of different heterobicyclic moieties (indazole, indole, imidazopyridine, and triazopyridine) by introducing a large number of mono- and di-substituted aromatic rings (phenyl, pyridine and dihydropyridine) or by replacing the type (carboxamide, inverse amide, methanimine, benzamide, and acetamide) and the position (C5 or C6) of the linker located between the heterobicyclic motif and the exocyclic aromatic ring (Fig. 2). Thus, several compounds of the structurally related substance classes of indazole-5-carboxamides, indole-5-carboxamides and (indazol-5-yl)methanimines were identified *in vitro* as best-in-class MAOIs that may now serve as promising lead structures or even as drug, radioligand, and diagnostic candidates, e.g., for the treatment of PD and other neurodegenerative diseases [32]. Among these new series, indazole-5-carboxamides were evaluated to be the most promising, selective and reversible inhibitors of human MAO-B, many of them with MAO-B activity in subnano- or even picomolar range and significantly improved *in silico* physicochemical and drug-like properties [32]. Consequently, further exploration has been performed within the series of indazole-5-carboxamides by introducing a lipophilic methyl and methoxyethyl

substituent either at the N1- or N2-position of the indazole moiety. The 3,4-dihalo-gen-substituted phenyl residue and the carboxamide linker were kept constant (Fig. 2). A similar inhibitor construction is also present in previously reported 5-carboxamidoindole derivatives with a reversed carboxamide linker [27,33]. However, the herein presented scaffolds realize very favorable water interactions by an amide flip and the introduction of an indazole N2 atom, entailing a pronounced affinity increase.

In the present study we report a series of structurally optimized *N*-alkylated indazole-5-carboxamide derivatives. All these compounds contain common pharmacophoric features: a hydrophobic 3,4-disubstituted-phenyl unit (Ph), hydrogen bonding domains (HBD, a carboxamide linker with hybrid character) and additional electron donor nitrogens (ED) in the indazole moiety. The compounds were tested at rat and human MAO A and B and, depending on the substitution pattern of the indazole N1- or N2-position, they may act either as selective MAO-B or dual MAO-A/B inhibitors with reversible mode of action. To find a plausible explanation for their high affinity and the observed differences in selectivity, docking experiments were performed using a novel modeling technology platform using X-ray structures of selected compounds under study. Moreover, we evaluated the drug-like and *in vitro* ADME properties of the studied compounds, including their water-solubility, logD, blood-brain-barrier (BBB) penetration, and gastrointestinal (GI) permeability.

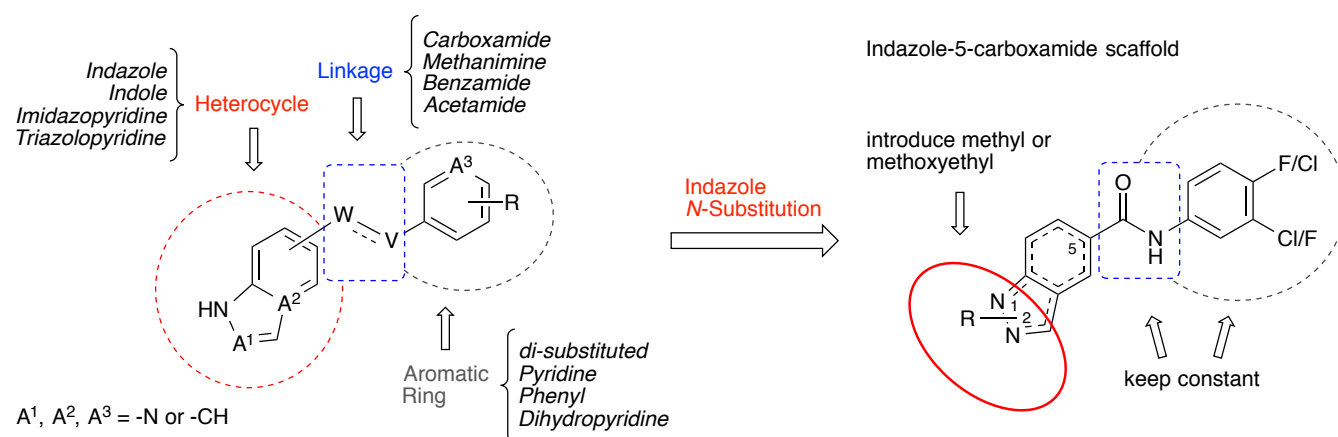
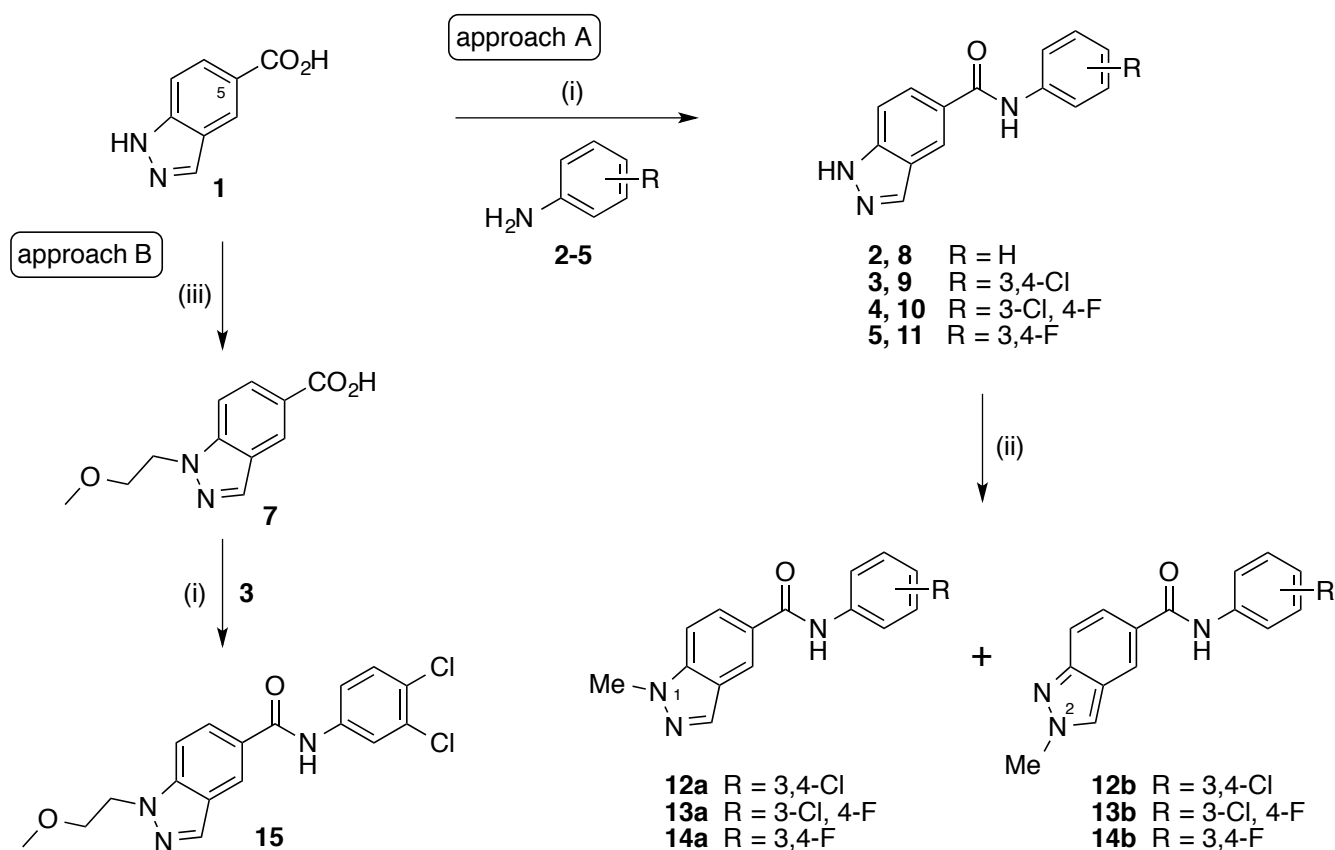


Fig. 2. Generic structure of previously discovered selective MAO-B inhibitors [31] (left) and intended chemical modifications of the indazole-5-carboxamide scaffold subjected in this work (right).

2. Results and discussion

2.1. Chemistry

Synthetic routes and chemical structures of the investigated compounds are shown in Scheme 1. Following our synthetic strategy for the formation of *N*-alkylated indazole-5-carboxamide derivatives possessing different alkyl substituents either at the indazole nitrogen atom 1 or 2, respectively, we started from the commercially available 1*H*-indazole-5-carboxylic acid (**1**). The advantage of this methodology consists in the introduction of the corresponding *N*-alkyl substituent either in the very last or in the first synthetic step, namely preparation of **12a,b–14a,b** (convergent approach A) and **15** (regioselective approach B) by only two or four steps, respectively.



Scheme 1. Synthetic routes to N1- and N2-substituted derivatives **12a–14a**, **12b–14b** and **15**. Reagents and conditions: (i) EDC–HCl/DIPEA, DMF, r.t., 3–16 h; (ii) for **9–11**: MMS (method 1) or MeI (method 2), K₂CO₃, DMF, r.t., 3–20 h; (iii) 1) MeOH, c. H₂SO₄ (10 mol-%), 1–3 h, 65–70 °C, 2) 1-bromo-2-methoxyethane, K₂CO₃, DMF, reflux, 9–16 h, 3) 2M NaOH, THF–H₂O (1:1), 30–35 °C, 1–3 h.

The preparation of indazole-5-carboxamide derivatives **8–11** was performed following a known procedure [31], but in this work we used optimized reaction conditions leading to **8–11** in higher yields (81% yield in average). The carboxylic acid **7** was prepared following a three-step reaction procedure (for details, see Supporting Information). Amide coupling was carried out by reaction of **1** and **7** with 3,4-disubstituted anilines **2–5**. The subsequent alkylation of **9–11** was performed with methyl methanesulfonate (MMS, method 1) and methyl iodide (method 2) as alkylating reagents, yielding regioisomeric mixtures of the corresponding N1- and N2-methylated products **12a,b–14a,b**. To improve the product yields and regioselectivity, the reaction was conducted with several modifications and improvements [34]. Higher yields of **12a,b–14a,b** (71% combined yield in average) were obtained when using MMS (method 1), whereas higher regioselective formation (preference for N1- vs. N2-substitution of the indazole moiety, see Table 1) was achieved by methylation of **9–11** with methyl iodide (method 2). The final products **12a,b–14a,b** were separated from their *N*-methylated mixtures by preparative RP18-HPLC. Product **15** was purified chromatographically. The optimized procedures allow the introduction of broad structural modifications, e.g., by a variation of the alkylation reagents and the differently substituted anilines, and therefore, an easy access to compound libraries for rapid evaluation of structure-activity and structure-selectivity relationships (SARs and SSRs).

In addition, we obtained the X-ray structures of **9**, **11**, **12a**, and **13b**, which confirmed the assumed preference of the 1*H*-indazole tautomeric form of the *N*-unsubstituted compounds **9** and **11**, as well as the methylation at the N1-position in **12a** and **13a** (for more details, see Section 2.3).

Table 1 N1- vs. N2-regioselectivity and yields for the alkylation of **9–11**.

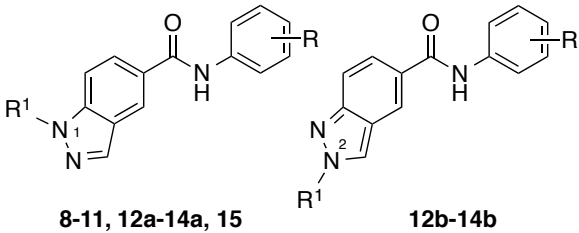
Starting compd.	Method	N1/N2 product mixture	N1/N2 ratio ^a	Combined yield (%) ^b
9	1 ^c	12a/12b	2.8 : 1	71
	2 ^d		4.7 : 1	56
10	1	13a/13b	2.7 : 1	72
	2		4.5 : 1	59
11	1	14a/14b	3.1 : 1	72
	2		4.3 : 1	61

^a Product ratio was determined by quantitative LC/ESI-MS of the isolated product mixtures. ^b Isolated yields refer to **1**.

^c Method 1: alkylating reagent MMS. ^d Method 2: alkylating reagent MeI.

2.2. Monoamine oxidase studies

The compounds were tested for their inhibitory activities on rat and human MAO-A and MAO-B using mitochondria-enriched rat liver fractions and microsomes of baculovirus-infected insect cells (BTI-TN-5B1-4) as sources for the rat and human recombinant MAO isoforms, respectively [31]. The evaluation of the enzyme inhibition of the test compounds against MAO-A and MAO-B isoforms was performed by a fluorescence-based assay [35] with the common substrate *p*-tyramine measuring the compounds' effects on the production of hydrogen peroxide (H₂O₂) using the commercial assay kit Amplex Red [36]. The two-step reaction for the determination of MAO activity involves an H₂O₂-production via oxidative deamination of *p*-tyramine by MAO (step 1) and a subsequent horseradish peroxidase (HRP)-catalyzed oxidation of the non-fluorescent and highly sensitive 10-acetyl-3,7-dihydroxyphenoxazine (Amplex Red reagent) by H₂O₂ to produce a fluorescent product, resorufin (step 2). The ratio of resorufin production is equal to the ratio of *p*-tyramine that is oxidized by MAO to the corresponding 2-(4-hydroxyphenyl)acetaldehyde in the above two-step reaction. To irreversibly block the respective isoenzyme in rat liver fractions, the inhibitors clorgyline (for MAO-A) and selegiline (for MAO-B) were applied for determining selective inhibition of the other isoenzyme [31]. These selective inhibitors, clorgyline and selegiline, were also used as positive controls in the corresponding MAO-A and MAO-B assays, respectively. Determined in vitro inhibitory potencies (IC₅₀ values) and selectivity toward hMAO-A and hMAO-B (expressed as selectivity index, SI) for all compounds and reference inhibitors are reported in Table 1. In addition, the kinetic parameters of hMAO-B (K_m and V_{max}) were determined under the above experimental conditions in the presence of different concentrations of *p*-tyramine (Fig. S2, Supporting Information).

Table 2 Monoamine oxidase activity of the tested compounds.


Compd.	R	R ¹	IC ₅₀ ± SEM (nM) ^a				SI ^b
			rat MAO-A	human MAO-A	rat MAO-B	human MAO-B	
8	H	H	>10000	>10000	708 ± 34	117 ± 13	>86
9	3,4-Cl	H	>10000	≥10000	1.43 ± 0.11	0.586 ± 0.087	17065
10	3-Cl, 4-F	H	>10000	>10000	2.36 ± 0.17	0.679 ± 0.044	14727
11	3,4-F	H	>10000	>10000	8.89 ± 0.05	1.59 ± 0.16	6289
12a	3,4-Cl	Me	>10000	>10000	1.32 ± 0.09	0.386 ± 0.052	25906
12b	3,4-Cl	Me	1740 ± 60	420 ± 24	22.5 ± 0.6	1.44 ± 0.41	292
12a/12b^c	3,4-Cl	Me	>10000	<10000	5.57 ± 0.65	1.87 ± 0.12	5348
13a (NTZ-1441)	3-Cl, 4-F	Me	>10000	≥10000	1.36 ± 0.13	0.662 ± 0.056	15106
13b (NTZ-1442)	3-Cl, 4-F	Me	1690 ± 143	562 ± 62	20.3 ± 3.0	8.08 ± 1.05	70
14a	3,4-F	Me	>10000	>10000	5.65 ± 0.48	1.52 ± 0.18	6579
14b	3,4-F	Me	1880 ± 93	764 ± 40	221 ± 21	38.4 ± 1.8	20
15	3,4-Cl	EtOMe	>10000	2870 ± 218	3.82 ± 0.22	1.08 ± 0.08	>2657
Moclobemide	–	–	10700 ± 700	361 ± 19 ^d	nt	nt	–
Safinamide	–	–	580000 (rat brain) ^e	45000 (human brain) ^e	18.0 ± 4.9 ^e	5.18 ± 0.04 ^e	5000

^a n = 3, unless otherwise noted. ^b Selectivity index: SI = IC₅₀(hMAO-A)/IC₅₀(hMAO-B). ^c Tested as a mixture of N1-/N2-isomers (N1/N2 ratio, 4.7:1). ^d Data are from ref. 37. ^e Data are from ref. 30. nt = not tested.

2.2.1. SARs and SSRs of indazole-5-carboxamide derivatives

The main goal of the present study was to evaluate the role and effects of the indazole N1- or N2-substitution with respect to the inhibition of both MAO-A and MAO-B enzymes. Based on their SARs and SSRs, the investigated compounds in Table 1 can be divided into three closely related chemical series as follows: *N*-unsubstituted indazole-5-carboxamides (designated subclass I, compounds **8–11**), N1-substituted indazole-5-carboxamides (subclass II, **12a–14a** and **15**), and N2-methyl-substituted indazole-5-carboxamides (subclass III, **12b–14b**). In general, all tested compounds show high inhibition of MAO-B ranging from low micromolar to picomolar potency. The biological evaluation of subclass I compounds was included to demonstrate the effect of the lipophilic phenyl residue on MAO inhibitory activity. Compounds of subclasses II and III were designed to further investigate the effects on inhibition potency and selectivity at both target MAO enzymes. A few substituents (mainly small lipophilic methyl groups) were also introduced at the position N1 or N2 of the indazole core to deeply understand SARs and SSRs of these new series of indazole-5-carboxamides. Evaluation of the biological data of all *N*-substituted compounds resulted in the identification of promising specific MAO-B (subclass II compounds) and dual MAO-A/B inhibitors (compounds of subclass III).

From all tested compounds, the *N*-unsubstituted compound **8** without substituents at the phenyl ring shows the lowest MAO inhibitory potency (human MAO-B, $IC_{50} = 117$ nM; rat MAO-B, $IC_{50} = 708$ nM). The introduction of electron-withdrawing groups (Cl and F) at the *meta*- and *para*-position of the phenyl ring in compound **8** resulted in remarkably potent and selective MAO-B inhibitors showing picomolar potency (subclass I compounds **9–11**). The 3,4-dichlorophenyl-substituted indazole-5-carboxamide **9** was found to be the most potent compound in this series (human MAO-B, $IC_{50} = 0.586$ nM; rat MAO-B, $IC_{50} = 1.43$ nM), being 9-fold more potent against human MAO-B than the standard inhibitor safinamide. The presence of 3-chloro-4-fluoro (compound **10**, human, $IC_{50} = 0.679$ nM; rat, $IC_{50} = 2.36$ nM) and 3,4-difluoro substituents (compounds **11**, human, $IC_{50} = 1.59$ nM; rat $IC_{50} = 8.89$ nM) led to highly potent inhibitors of human and rat MAO-B, the potencies of which are comparable to

those of the parent compound **9**. Compared to safinamide, compounds **10** and **11** display a >7- and >3-fold increase in inhibitory potency toward hMAO-B, respectively.

Following our rational design strategy, we used the 3,4-dihalophenyl-substituted indazole-5-carboxamides **9–11** as basic structures for further modifications of the indazole N1 and N2 positions. As a next step, the indazole N1 atom was substituted to obtain the N1-alkyl-substituted regioisomers **12a–14a** and **15**. The N1-methylated derivatives **12a–14a** proved to be extremely potent and selective inhibitors of MAO-B with slightly increased potency when compared to their *N*-unsubstituted analogs **9–11**. Methylation at the indazole N1 position in **9** provided the most potent MAO-B inhibitor (compound **12a**) of all compounds investigated (human, $IC_{50} = 0.386$ nM; rat, $IC_{50} = 1.32$ nM; SI = 25906), being ~2-fold more potent than the parent compound **9**. The N1-methylated 3-chloro-4-fluorophenyl- and 3,4-difluorophenyl derivatives **13a** (human, $IC_{50} = 0.662$ nM; rat, $IC_{50} = 1.36$ nM) and **14a** (human, $IC_{50} = 1.52$ nM; rat, $IC_{50} = 5.65$ nM) display equally high activity against rat and human MAO-B and selectivity versus MAO-A (**13a**, SI = 15106; **14a**, SI = 6579) compared to the potency and selectivity of the corresponding *N*-unsubstituted compounds **10** and **11**. It should be noted that for **12a–14a** (subclass II compounds) the 3,4-dihalophenyl-substituted phenyl ring has the same effect on MAO-B inhibitory activity and selectivity as observed for *N*-unsubstituted indazole-5-carboxamides **9–11** (subclass I compounds). The IC_{50} values and SI slightly decrease within both subclasses in the rank order as follows: 3,4-di-Cl (**9**, **12a**) \approx 3-Cl, 4-F (**10**, **13a**) > 3,4-di-F (**11**, **14a**). This observation could be explained with a decrease in the lipophilic character (Cl vs. F) of these compounds (cp. the modeling studies below). Next, we continued with the modification of the indazole N1 position in **9** by introducing of a larger methoxyethyl substituent (compound **15**). In comparison to the N1-methyl-substituted indazole-5-carboxamides and the unmethylated lead structure **9**, compound **15** is similarly potent against MAO-B (human MAO-B, $IC_{50} = 1.08$ nM; rat MAO-B, $IC_{50} = 3.82$ nM) and approximately 5-fold more potent than safinamide. Moreover, compound **15** was also identified as the only example in this series exhibiting notable inhibitory activity at human MAO-A ($IC_{50} = 2870$

nM), whereas at rat MAO-A it is essentially inactive (10 μ M). The N1-methoxyethyl substitution of the indazole moiety was found to be preferable for MAO-B inhibition, **15** is still >2657-fold selective for human MAO-B over human MAO-A. Our results suggest that the active site of human MAO-B in the substrate cavity region (within a close vicinity to FAD of about 3-4 Å) is able to accommodate lipophilic substituents with an appropriate length up to four atoms at the indazole N1 position. Consequently, the indazole N2 position in compounds **9–11** was methylated producing N2-methylated regioisomers **12b–14b** (subclass III). All of them were found to be dual MAO A and B inhibitors with low to subnanomolar potencies against hMAO-B and moderate nanomolar potencies against hMAO-A. Compared to their N1-methylated regioisomers **12a–14a**, the potency at rat and human MAO-B decreased, while an increase of the inhibitory activity against rat MAO-A (IC_{50} = 1.74, 1.69, and 1.88 μ M) and human MAO-A (IC_{50} = 420, 562, and 764 nM) was observed for N2-methylated analogs **12b–14b**, respectively. Compound **12b** was identified as the most potent *dual* MAO-A/B inhibitor in this series (human MAO-B, IC_{50} = 1.44 nM; human MAO-A, IC_{50} = 420 nM) with ~15-fold higher affinity for the human than for the rat MAO-B enzyme (rat MAO-B, IC_{50} = 22.5 nM), displaying the major species differences of all investigated compounds. The N2-methylated compounds **13b** and **14b** are less potent than the corresponding N1-substituted isomers **13a** and **14a** and the unmethylated analogues **10** and **11**, but they are still highly potent against human MAO-B (**13b**, IC_{50} = 8.08 nM; **14b**, IC_{50} = 38.4 nM). Compounds **12b** and **13b** show MAO-B and MAO-A inhibitory potencies when compared to the standard reversible inhibitors moclobemide (MAO-A) and safinamide (MAO-B), respectively. Thus, the N2-methyl substitution of the indazole moiety was evaluated to be beneficial for inhibition of human MAO-A with preferences for MAO-B over MAO-A isoenzyme (**12a**, SI = 292; **13b**, SI = 70; **14b**, SI = 20). Finally, a mixture of both most potent N1- and N2-methylated regioisomers **12a** and **12b** (4.7:1 ratio) was tested in order to evaluate the combined effect of the indazole N1 and N2 substitution on MAO-B inhibitory activity and selectivity against MAO-A. The mixture of **12a** and **12b** showed high MAO-B inhibitory potency (human MAO-B, IC_{50} = 1.87 nM; rat MAO-B, IC_{50} = 5.57 nM), being

>5000-fold selective for human MAO-B over human MAO-A. On the basis of its high bioactivity, which was comparable to the single N1- and N2-methylated isomers **12a** and **12b**, such mixture may as well be considered for further development of radioligands.

2.2.2. Species differences

Meaningful species differences and clear correlations between rat and human IC_{50} values were previously described not only for subclass I compounds, but also for other related classes MAO-B inhibitors [30]. In order to access the species selectivity, all compounds were tested at rat and human orthologs of MAO-A and B. As shown in Fig. 3, significant differences in inhibitory potencies (expressed as pIC_{50}) at rat and human MAO-B for compounds of all three series could be noticed. A good correlation between rat and human MAO-B inhibitory activity could be observed when all determined pIC_{50} values at rat MAO-B versus pIC_{50} values at human MAO-B isoform were plotted. Linear regression gave a slope of 1.10, y-intercept equal to -1.47 , and $R^2 = 0.93$ (Fig. S3, Supporting Information). Compounds of subclasses I and II were virtually inactive at MAO-A at the highest concentration tested ($10 \mu\text{M}$). Therefore, species differences at MAO-A could only be observed for the N2-methylated indazole-5-carboxamide derivatives **12b–14b** (subclass III compounds). Overall, the potency of the compounds at human MAO isoforms was noticeably higher than at their rat orthologs. The N2-methylated derivatives **12b** and **14b** showed the highest deviation between the pIC_{50} values at rat and human MAO-B (~ 1.2 log units for **12b**) and the pIC_{50} values at rat and human MAO-A (> 1.4 log units for **14b**), respectively. Considering that a similar trend in species differences was observed for structurally related compounds [32], it will be required to determine MAO inhibition of both A and B isoforms first against the human enzyme and, only for selected compounds, against their rat orthologs before starting preclinical and *in vivo* clinical studies.

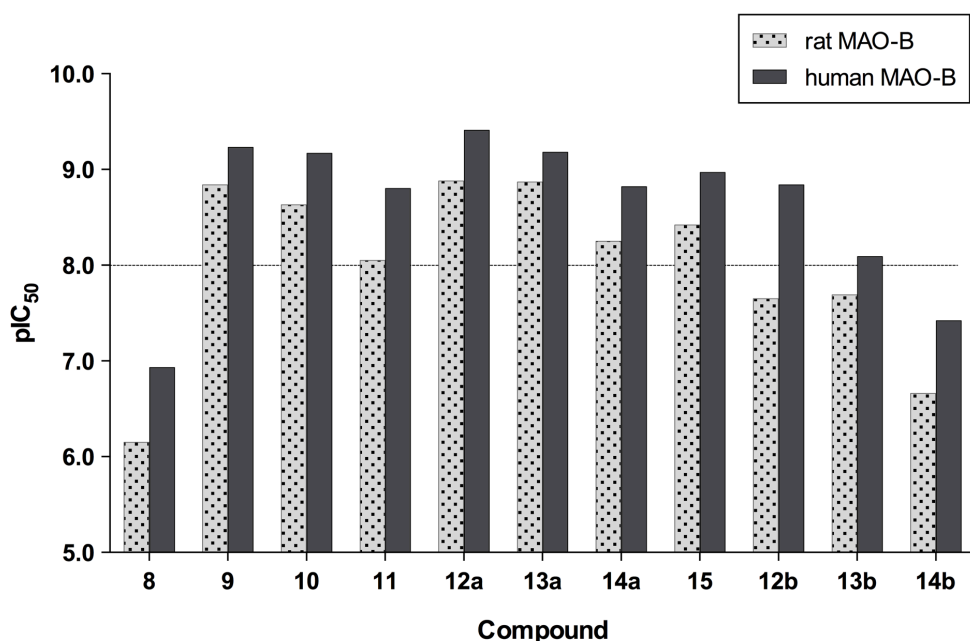


Fig. 3. Rat vs. human MAO-B pIC₅₀ values distribution within the series of indazole-5-carboxamides **8–15**. Almost all compounds are highly potent MAO-B inhibitors (pIC₅₀ > 8.00).

2.3. Crystal structures

2.3.1. Crystal structures of **9** and **11**

In order to understand the rationale behind the MAO inhibitory and selectivity properties of *N*-substituted indazole-5-carboxamides (subclass II and III compounds), our first step was to determine the single crystal molecular X-ray structures of selected *N*-unsubstituted precursors **9** and **11** as well as *N*-1-methylated derivatives **12a** and **13a**, and to evaluate their specific inter- and intramolecular interactions within the respective crystal units (see Experimental Section and Supporting Information).

An overview of the X-ray structural analysis of compounds **9** and **11** with atom numbering is shown in Fig. 4. The crystal structure of **9** confirms its almost planar conformation. The two fused five- and six-membered rings are forming together the first plane of the molecule, maximum deviation from the mean plane of the indazole moiety shows C13 with 0.015(1) Å. A second plane, defined by C1-C6 of the planar 3,4-dichlorophenyl-ring, is tilted by 3.67(3)° against the first one, the nitrogen atom N1 deviates 0.08(1) Å from this plane. The aromatic and indazole units are connected by a carboxamide

linkage with torsions of $177.7(1)^\circ$ (C8-C7-N1-C5) and $-1.2(2)^\circ$ (O1-C7-N1-C5). The angles are $121.5(1)^\circ$ (O1-C7-C8) and $122.7(1)^\circ$ (N1-C7-O1). The plane defined by the carboxamide linker (C5, N1, C7, O1, C8) encloses an angle of $32.16(4)^\circ$ with the indazole moiety and an angle of $33.09(5)^\circ$ with the phenyl ring. To investigate the ability of indazole-5-carboxamides to form intermolecular hydrogen bonds under conditions that mimic the biological targets of interest, e.g., MAO A and B enzyme, we studied the effect of water and different solvents on the conformational changes and tautomerism of the indazole moiety in **11**. Therefore, crystals suitable for X-ray structural analysis were obtained after slow recrystallization of **11** from a methanol–water mixture (2:1) as well as methanol and acetonitrile solvents at room temperature (RT). The X-ray structure of **11** reveals a different rotamer compared to **9** (Fig. 4B). The indazole and phenyl rings are not co-planar but tilted by $62.12(4)^\circ$ (in **9**: 3.67°), which is clearly demonstrated by an overlay of the indazole moieties of **9** and **11** (Fig. 5). A solvent-dependent rotamerization of **11** was not observed. The deviation of C7 atom from the best plane of the indazole moiety is $0.01(1)$ Å. The respective torsions ($176.4(2)^\circ$ and $-3.1(2)^\circ$) and the angles ($121.5(1)^\circ$ and $123.0(1)^\circ$) of the carboxamide linkage are similar to those observed in the crystal structure of **9**. The plane defined by the carboxamide linker (C5, N1, C7, O1, C8) encloses an angle of $25.42(4)^\circ$ with the indazole moiety and an angle of $36.85(5)^\circ$ with the phenyl ring. Relevant structural data for all single X-ray structures in the present work are listed in Table S9 (see Supporting Information).

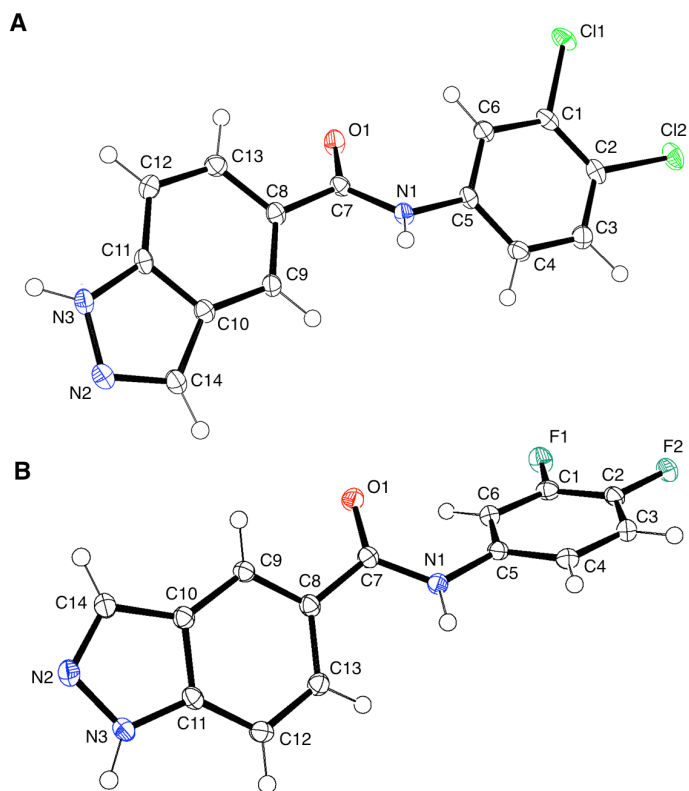


Fig. 4. Single X-ray structures of compounds **9** (A) and **11** (B) showing the atom numbering. The thermal ellipsoids are drawn at the 50% probability level.

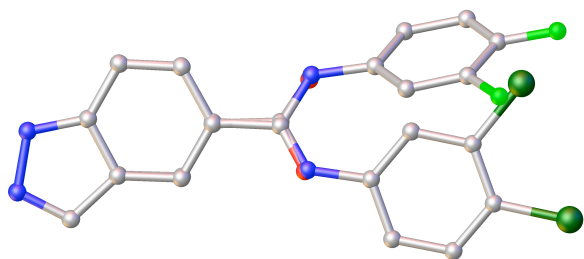


Fig. 5. Overlay of compounds **9** and **11** showing the different rotamers. Hydrogen atoms are omitted for clarity.

In comparison to the crystal structure of **9**, the indazole moiety, the phenyl residue, and the carbonyl group in **11** have another orientation to each other indicating of a rotamerization (rotation around the carboxamide bond C8–C7), resulted probably by intermolecular interactions in the crystal by hydrogen bonds (Fig. S3, Supporting Information). Both compounds build a chain by hydrogen bridging between H1 and O1 by translation of the molecule along the *b* axis with N–H...O distances of 2.07(2) for **9** and

2.26(2) Å for **11**. Additional hydrogen bridges can be found between N3-H3 and N2 generated by a two-fold screw axis with N-H...N distances of 2.03(2) Å resp. 2.00(2) Å, thus both molecules form double chains.

The molecules adopt an antiparallel orientation; the plane-to-plane angle defined by the mean plane of all atoms of an individual molecule is of 75.9(2)° for **9**. For **11**, the plane-to-plane angle defined by the atoms of the indazole moiety was 60.2(1)°. As can be seen from Fig. S3 the different rotamers shows similar double chains, the difference lies direction of the second N-H...N hydrogen bond compared to the first one: In **9** they point into opposite directions, in **11** they point into the same direction. Our results suggest that the carboxamide linker in **9** and **11** play an important role for the formation of hydrogen bonds due to its conformational and hybrid features (hydrogen bond acceptor/donor) allowing structural flexibility of indazole-5-carboxamides within the MAO enzymes, i.e., under physiological conditions (e.g., pH 7.4 at ~37 °C). Moreover, the X-ray analysis of **9** and **11** indicates that the comparably high MAO-B inhibitory activity of *N*-unsubstituted indazole-5-carboxamides (subclass I) is due to their stable *1H*-indazole and keto tautomeric forms. Otherwise, a *2H*-indazole and/or keto-enol tautomerism would be observed in the case of compound **11**, which was recrystallized in the presence of water (see also Section 2.5 and Experimental Section).

2.3.2. Crystal structures of compounds **12a** and **13a**

The X-ray structural analysis of compounds **12a** and **13a** with the atom numbering is shown in Fig. 6. Single crystals of **13a** were twinned with a ratio of 59:41 by a rotation of 180° around the [001] direction. Similarly to **9**, the crystal structures of **12a** and **13a** confirm their almost planar conformation. The two fused five- and six-membered rings in the indazole moiety are almost coplanar; no atoms of these units show a deviation of more than 0.02 Å out of that plane. The deviation of the carbonyl C7 and the methyl C15 atoms are 0.12(1) Å respectively 0.07(1) Å for **12a** and 0.15(1) Å respectively 0.16(1) Å for **13a**. The second plane, defined by the phenyl ring, is tilted by 6.01(5)° (in **12a**) and 5.7(1)° (in **13a**) against the first one (Fig. 6).

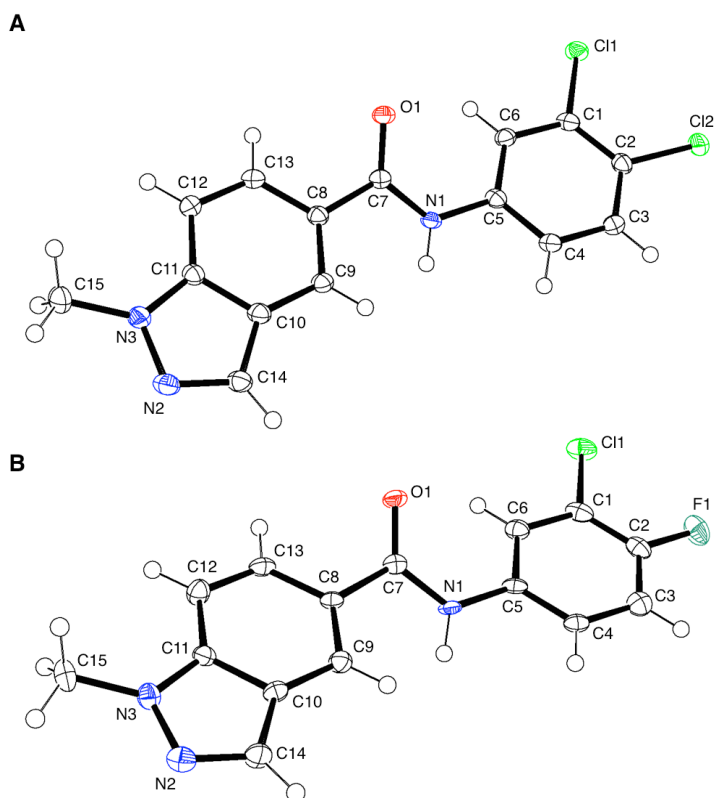


Fig. 6. Single X-ray structures of compounds **12a** (A) and **13a** (B) showing the atom numbering. The thermal ellipsoids are drawn at the 50% probability level.

The nitrogen atom N1 resides nearly perfectly in the plane of the phenyl ring (deviation 0.02(2) Å and 0.01(1) Å, respectively). Interestingly, the plane defined by the carboxamide linker is tilted versus both ends, namely 27.5(1)° to the indazole moiety and 28.3(1)° to the phenyl ring in **12a**. The corresponding values are 29.1(1)° and 30.5(1)°, respectively, in **13a**. The bond angles and lengths of the carboxamide linker in all X-ray structures are almost identical (cp. Table S9). As well as the intermolecular patterns of **9** and **11** for both structures, intermolecular hydrogen bonds can be found between H1 and O1 generated by translation along the *b* axis forming chains with H...O distances of 2.17(3) Å in **12a** and 1.99(4) Å in **13a** (Fig. S4). Because of the lack of a second N-H donor compared to **9** and **11**, no comparable anti-parallel double chains are formed. This conformation does not prevent the carboxamide linkage to build geometrically sound intermolecular hydrogen bonds. The intermolecular interaction geometries of compounds **9**, **11**, **12a** and **13a** are collected in Table S10.

2.4. Molecular Modeling Studies

2.4.1. Docking of compounds **12a**, **12b**, **13a**, and **13b** into human MAO-B

SAR and SSR evaluation of indazole-5-carboxamide analogs reported herein, including the X-ray analysis of compounds **9**, **11**, **12a** and **13a**, as well as previous docking studies with the structurally related indole-5-carboxamide derivative NTZ-1010 [39] provided valuable information about the binding modes determining their MAO-B inhibitory potency. The co-crystal X-ray structures of both hMAO-A and hMAO-B enzymes with the reversible inhibitors harmine (PDB code: 2Z5X) [40] and safinamide (PDB code: 2V5Z) [41] provided insight into the structural features of these key biotargets for the research in the field of MAO inhibition in relation to their therapeutic use in neurological disorders.

As a next step it occurred therefore natural to select the N1-methylated compounds **12a** and **13a** as well as their N2-methyl-substituted derivatives **12b** and **13b** for molecular modeling experiments. After a successful applicability check of the methods applied (re-docking and scoring), we investigated their binding situation and rationalized the most significant interactions and desolvation effects within the substrate active site of hMAO-B (**12a,b** and **13a,b**) and hMAO-A (**12b** and **13b**). The results shall provide additional information including (i) an explanation for the observed preference in inhibitory potency at hMAO-B isoform of N1- versus N2-methyl-substituted regioisomers (**12a** and **13a** vs. **12b** and **13b**), on the one hand side, and versus safinamide on the other, (ii) a semi-quantification and visualization of the hydrophobic effects and enthalpic and entropic binding, (iii) an exploration of the unoccupied space within the substrate cavity region of hMAO-B for further development of CNS drugs, and (iv) proposals of binding modes of dual MAO-A/B active compounds **12b** and **13b** within the binding site of the human MAO-A isoform. Binding modes were computed with LeadIT [42], free energy of binding estimates were calculated and visualized with the software SeeSAR [43] using a novel, yet well-validated computational free energy approximation "HYDE" in combination with single X-ray analysis [44]. Since biological data showed a species-dependent preference in inhibitory potency

for human versus rat MAO orthologs, the modeling studies were run on the human model of the MAO-A and MAO-B enzyme (see Experimental Section). Given their availability, the docking experiments were performed with the ligands' single X-ray structure geometries (i.e., bond lengths and angles) of **12a** and **13a** without further preparation, leading to an excellent agreement between experiment and computation (cf. Supporting Information). The selected docking solutions of N2-methylated compounds **12b** and **13b** were guided using co-visualization with their N1-methylated isomers **12a** and **13a** within the binding site of the hMAO-B enzyme.

On the basis of the docking model and previous observations [30,39], the binding pocket of human MAO-B can be divided into three different subpockets inside the protein from the ligands perspective: (i) an indazole binding region is anchored in the "substrate cavity" and oriented toward the FAD with a postulated H-bond 1 between the N2 atom and the water molecule 1180 (designated subpocket I, S1), (ii) a linker region with a postulated H-interaction 2 between the oxygen of the carbonyl group and the water molecule 1247 (subpocket II, S2), and (iii) a highly lipophilic halogen binding subpocket (hydrophobic subpocket III, S3) located in the "entrance cavity" of the human MAO-B enzyme (Fig. 7 and 8). Furthermore, the binding modes and estimated affinities strongly suggest that **12a,b** and **13a,b** occupy the same substrate cavity space as previously determined for the *N*-unsubstituted compound **9** [30], provided that both ligands do not covalently bind with the FAD cofactor. Compounds **12a** and **13a** differ from **9** by a methyl substitution at N1 and, therefore, their binding poses show some significant features with respect to the orientation of the indazole scaffold in **9** within the subpocket S1. The X-ray analysis of **9** and re-assessing the geometries with SeeSAR resulted in a similar conformation to the ones of the N1-methyl analogs **12a** and **13a**, which results from a rotation on the C8-C7–N1-C5 torsion angle of about 180° (cp. Fig. S6).

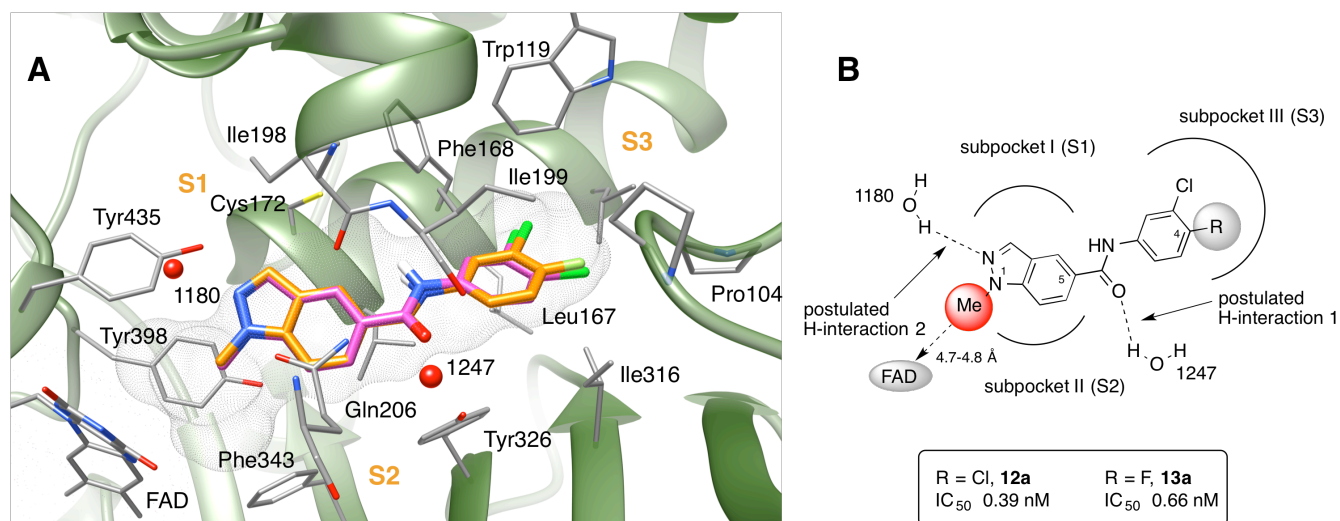


Fig. 7. (A) Binding modes of **12a** (magenta sticks) and **13a** (orange sticks) overlaid onto the crystal structure of the hMAO-B/safinamide complex (PDB: 2V5Z). The main surface area of safinamide is shown as a grey mesh. For clarity, only the relevant residue side chains and the FAD cofactor are shown in grey sticks; all water molecules except HOH1180 and HOH1247 (red spheres) were removed. The crystal structure of MAO-B is represented as ribbons. Clipping planes have been used for better visibility [45]. (B) 2D binding model for **12a** and **13a** differ only by the halogen substitution (Cl vs. F, light grey sphere) in the 4-position of the phenyl ring. The postulated H-interactions 1 and 2 are displayed as dashed lines. The dashed arrow between the FAD cofactor (grey ellipse) and the N1-methyl substituent (red sphere) indicates a favorable orientation of the indazole moiety within the active binding site of hMAO-B.

In addition to the N1-methyl substitution, the indazole N2 atom and the carboxamide linker of **12a** and **13a** are suggested to play an essential role for their conformation within the substrate cavity region of hMAO-B (subpocket I and II) interacting favorably with the water molecules 1247 (CO---HOH1247 ≈ 1.8 Å) and 1180 (N2---HOH1180 ≈ 1.9 Å), respectively (Fig. 7B). Finally, the 3,4-dihalo-substituted phenyl ring of the ligands occupies a strongly hydrophobic binding pocket in the models (subpocket III) dominated by hydrophobic effects (see the HYDE analyses below). There are a multitude of hydrophobic amino acids, notably leucin, isoleucin and proline residues. In summary, we computed that for this subclass of N1-methyl indazoles the two relevant H-bonds are highly coordinated also by protein residues (for HOH1247: GLN206, ILE199, TYR201 and 326; for HOH1180: CYS172 and TYR188), making them more essential for the ligand stabilisation (CO---HOH1247) and conformation (N2---HOH1180) in the binding site through non-covalent interactions.

From earlier HYDE analyses it emerged that N2 is the only atom contributing slightly unfavorably in the *N*-unsubstituted indazoles [30], it appeared therefore natural that an option for further optimization of this class of compounds could proceed from, for example, a vector at this very "water-like" N2 position. This computed proposal is now experimentally backed by the N2-methyl indazole regioisomers **12b–14b** (subclass III compounds), which are not only well tolerated by human MAO-B, but also showed a moderate activity for the human MAO-A isoenzyme. With the aim to deeper understand why the N1-methyl-substituted indazoles exhibit higher affinity towards human MAO-B than their N2-methylated regioisomers (e.g., more than one log unit K_i difference between **13a** and **13b**), we compared compounds **12a** and **13a** with their respective N2-methylated isomers **12b** and **13b**. For this purpose, we computed the binding models of **12b** and **13b** on the structural basis of their N1-methylated analogues using the new 3D structure editor in SeeSAR v5 (Fig. 8).

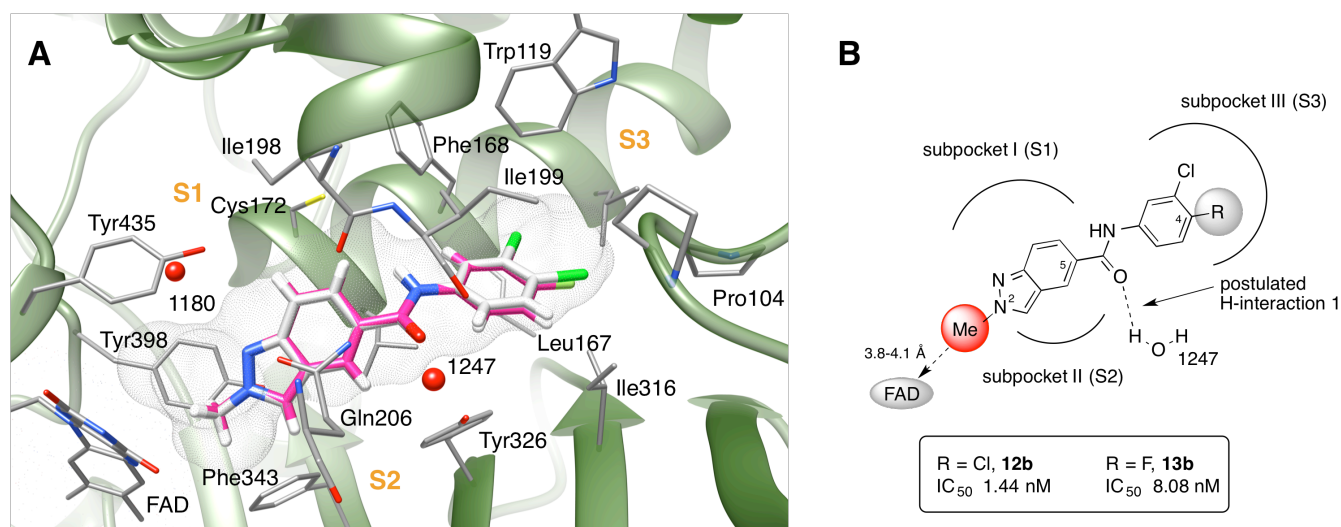


Fig. 8. (A) Binding modes of **12b** (grey sticks) and **13b** (pink sticks) overlaid onto the crystal structure of the hMAO-B-safinamide complex (PDB: 2V5Z). The main surface area of safinamide is shown as a grey mesh [45]. (B) 2D binding model for **12b** and **13b** differ only by the halogen substitution (Cl vs. F, grey sphere). The dashed arrow between the FAD cofactor (grey ellipse) and the N2-methyl substituent (red sphere) indicates a favorable orientation of the indazole moiety within the active binding site of hMAO-B.

Similarly, compounds **12b** and **13b** share analog binding mode motifs in the active binding site as observed for **12a** and **13a** (cp. above) and also comparable desolvation effects. However, there are some

differences in ligand-receptor interactions and desolvation contributions observed in particular for (i) the N2-methyl group and (ii) the neighboring N1 position in the indazole moiety: Here again, the indazole-binding site of the pocket is limited by the FAD cofactor (Fig. 8B).

The N2-methyl group of **12b** and **13b** is closer to the FAD co-factor than for the N1-methylated analogs **12a** and **13a** (distance to the flavin C4 and C4a atoms of about 3.8–4.1 Å). Furthermore, the N2-indazole methyl group in **12b** and **13b** occupies the hydrophobic subpocket favorably – yielding a HYDE contribution of approximately –6 kJ/mol (i.e., approx. –2 kJ/mol lower than for **12a** and **13a**). In the case of an indazole N2-methyl substitution, we observed only one H-bond between water 1247 and the carboxamide linkage (CO---HOH1247 \approx 1.8 Å) and hydrophobic contacts with the amino acids ILE199 and TYR326 (for details, see Table S11 in the Supporting Information). In conclusion, the N1- (**12a** and **13a**) and N2-methyl-substituted indazoles (**12b** and **13b**) exhibit slightly different binding affinities towards human MAO-B enzyme (e.g., **12a**, IC₅₀ = 0.39 nM; **12b**, IC₅₀ = 1.44 nM; **13a**, IC₅₀ = 0.66 nM; **13b**, IC₅₀ = 8.08 nM) due to their different entropic contributions (hydrophobic/desolvation effects) to the total binding energy and an additional H-interaction (enthalpic effect) at the N2 position in **12a** and **13a**. Compared to the N1-methyl substitution, the N2-methyl group has a slightly different space orientation in the FAD cleft that might be to avoid clash and, therefore, to a regiochemically unfavorable "switched" conformation within the active site of hMAO-B. Furthermore, it is well known that unfavorable desolvation effects may well lead to a decreasing in potency, even though the tightness of fit is good [46].

Regrettably, there are no co-crystal structures of **12a,b** and **13a,b** available today to confirm these models experimentally. However, we have good belief in the modeled binding modes for the following reasons: (i) the cores of **12a,b** and **13a,b** are in exactly the same binding region as observed for safinamide in X-ray structures before, and (ii) the trends of affinity are correctly described: The unsubstituted phenyl analog **8** shows an approximately 177- and 15-fold reduced hMAO-B activity in the experiment compared to **13a** and **13b**, respectively. This is in (quantitative) agreement with the

HYDE predicted contribution of the two halogen atoms of **13a** (approx. -14 kJ/mol) and **13b** (approx. -13 kJ/mol), corresponding to a contribution of almost three orders in magnitude of the K_i values (Fig. 9).:-

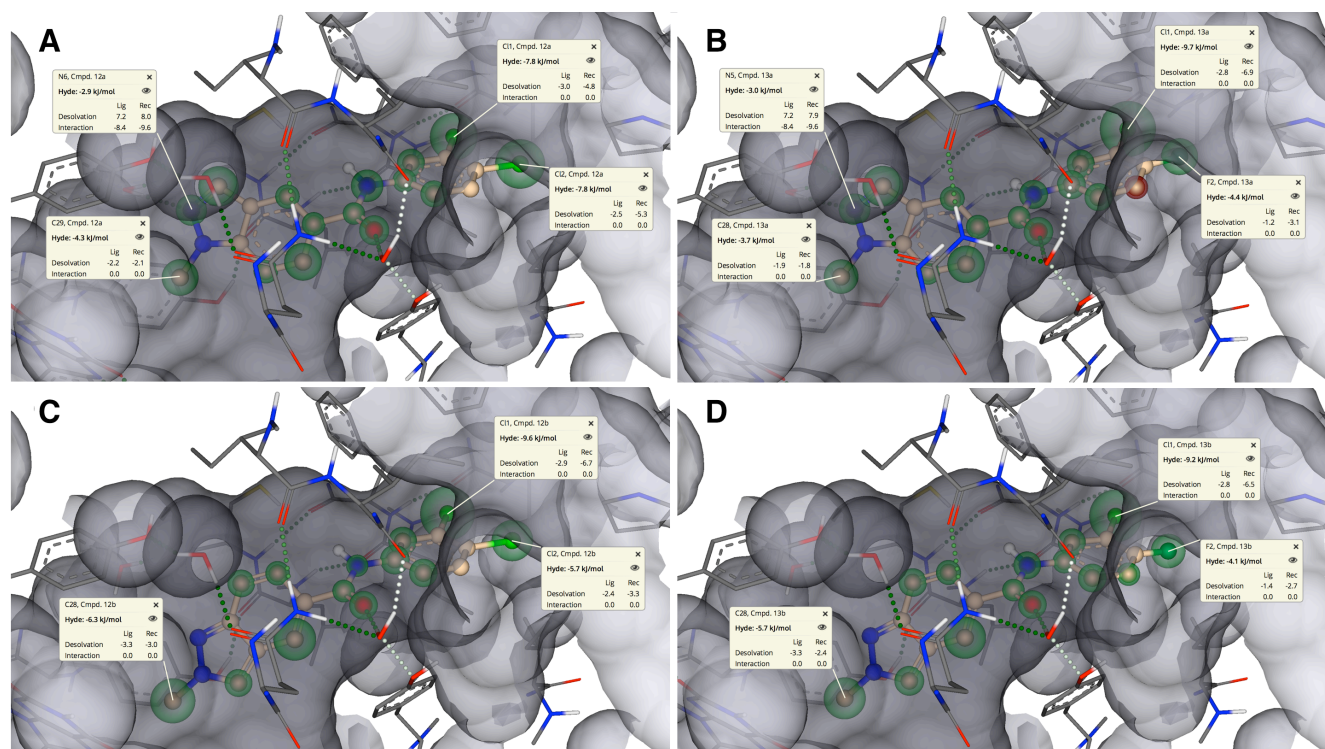


Fig. 9. SeeSAR visualization of the binding of compounds **12a** (A), **13a** (B), **12b** (C), and **13b** (D) to human MAO-B (PDB: 2V5Z). HYDE visual affinity assessment: green = favorable, red = unfavorable and non-colored = no relevant for affinity. The ligand, protein residues, water molecules and FAD are shown in the same orientation, color code and structure representation as in Fig. 7 and 8.

To gain insight into the *overall* binding thermodynamics of **12a,b** and **13a,b** to human MAO-B and, therefore, to find a plausible explanation for their preference in inhibitory potency versus safinamide, we applied HYDE scoring and visualization as embedded in SeeSAR. HYDE considers H-bonds (enthalpy) and dehydration ("desolvation", entropic) effects of all atoms using a united atom computation at the end (i.e., non-hydrogen atoms contain the hydrogen contributions); the atomic visualization as spheres ("HYDE coronas") reflects both the protein as well as the ligand energy terms. SeeSAR was applied after dockings (for details, see Fig. S7 and Table S12, Supporting Information) and entails an RMSD-limited pre-optimization towards clash-free and torsionally relaxed output. Our HYDE study was particularly focused on the estimation and visualization of the major ligand-receptor

interactions plus desolvation effect estimations at (i) the indazole N1- and N2-methyl function and (ii) the 3,4-dihalo-substituted phenyl ring, especially at the phenyl C4 position (chloro- vs. fluoro-substitution). The indazole-binding site of the pocket is limited by the FAD cofactor (cf. Fig. 7 and 8). The N1-methyl substitution, which entails a displacement of HOH1180, is computed as responsible for a slight affinity increase compared to safinamide alongside the effects of the respective 3,4-dihalophenyl substituents in **12a** and **13a**. The H-bond interaction between the indazole N2 atom and the water 1180 (ΔH of about -18 kJ/mol) is compensated by a desolvation "penalty" at TYR435 for both ligands (~ 15 kJ/mol) resulting in a HYDE contribution of this bond of about -4 kJ/mol for both ligands (cp. Table S11). In the case of safinamide, the water molecule 1192 and the residue GLN206 are involved in H-bond interactions with the NH_2 group in the α -aminoamide polar part – leading to a HYDE score of about -3.7 kJ/mol.

Since the fluorine atom is much smaller than the chlorine atom (cp. **12a**), the HYDE model predicts slightly less affinity for the fluoro compound **13a** (Fig. 9A and 9B). However, the error bars largely overlap – in other words, the computer cannot distinguish between the energies of the two. HYDE reveals -15.6 kJ/mol in total for both chlorine atoms at phenyl C3 and C4 positions in **12a**, whereas the scoring for **13a** provides a value of -9.7 kJ/mol for the chlorine and -4.4 kJ/mol for the fluorine at the phenyl C4 position, respectively. The sum of the desolvation effects for both halogens in **13a** is approximately -14.1 kJ/mol (i.e., -1.5 kJ/mol lower than calculated for **12a**). Further HYDE analyses provide similar contributions of the most important heavy atoms (e.g., amide spacer, N1, C6, C3 and methyl carbon atom) to the free energy for both compounds. The flexible carboxamide linkage between two lipophilic moieties in the indazole-5-carboxamides is crucial not only for the observed high MAO-B inhibitory potency (NH-C(=O) contribution of $\sim 5\text{--}6$ kJ/mol; also cp. the preferences for N1-methyl-substituted indazoles versus safinamide), but also acts like an 'anchor', steering the positioning of the hydrophobic parts in the pocket. Our HYDE analysis provides hints towards why there is better hMAO-B affinity of the N1-methyl indazole-5-carboxamides compared to safinamide, e.g., "red corona" at its

imine nitrogen and no favorable contributions at the ether carbon atom, versus the overall favorable contributions computed and visualized in **12a** and **13a** (cp. Fig. S6B). The thermodynamic profile computed by HYDE (that takes explicit, untrained account of *enthalpy-entropy compensation* [47,48 and references therein]) of safinamide to hMAO-B showed almost equal, favorable contributions of the enthalpic and entropic terms (approx. -20 kJ/mol each) to the total free binding energy (Fig. S7). Compounds **12a** and **13a** showed similar thermodynamic profiles with a predominant enthalpic contribution of -38 kJ/mol and favorable entropic terms of -9.9 and -7.5 kJ/mol, respectively. In contrast, the free energy of **12b** and **13b** is rather driven by desolvation (entropic) effects summing up to a favorable $-T\Delta S$ value of -25 kJ/mol (cp. Fig. S7). Finally, the results obtained from the HYDE analyses of compounds **9** and **11–13** reproduced their hMAO-B activities, which decrease in the following rank ordering: **12a** > **13a** \approx **9** > **12b** \approx **11** > **13b**.

The results obtained from the docking studies and HYDE analyses of N1- and N2-methyl-substituted indazole-5-carboxamides prompted us to further explore the potential of this promising class of MAO-B inhibitors for the development of CNS drug candidates. A detailed examination of their SARs and thermodynamic profiles suggested that a large hydrophilic substitution should make the indazole N1 position less accessible for water, entailing a "quenching" (downsizing) of unfavorable desolvation effects and, therefore entail an improvement of affinity with respect to the N2 alternation [32].

In this light, we compared the best docking poses of our compounds (**9–15**) computed in SeeSAR with those observed from the biological experiments. All final poses of the compounds were validated (number of docking poses per ligand $N = 5$) and visually inspected. The estimated affinities (SeeSAR's HYDE reports K_i ranges rather than values to avoid the illusion of a non-existing accuracy of our computations) of all selected poses lie in the nanomolar (or even better) affinity region – as confirmed by biological experiments (Table S13, Supporting Information).

Table 3 summarizes the experimental and computed affinity data for safinamide and compounds **9–15** at human MAO-B (K_i values in the (sub-)nanomolar range). There is a good overall agreement with the estimated affinity ranges, e.g., HYDE scores / K_i values (low nM). As expected from a visualization of the situation in SeeSAR, consistently, the N1-substitution appears to be highly more favorable (0.17 and 0.29 nM for N1 vs. 0.64 and 3.57 nM for N2, and 0.48 nM for **15** with N1, too).

Table 3 HYDE estimated affinity ranges and experimental K_i values for the inhibition of human MAO-B by safinamide and compounds **12–15**.

Compd.	N1-/N2-substitution	$K_{i\text{HYDE}}$ (nM) ^a	K_i (nM) ^b
12a	N1	0–37	0.17
12b	N2	1–123	0.64
13a	N1	1–103	0.29
13b	N2	1–148	3.57
15	N1	<6.05	0.48
Safinamide	–	2–179	2.29

^a Estimated HYDE K_i range values. ^b The K_i values were approximated from the experimentally measured IC_{50} values according to the equation by Cheng and Prusoff [49]: $K_i = IC_{50}/(1 + [S]/K_m)$ with $[S] = 150 \mu\text{M}$ and K_m (*p*-tyramine) = 118.8 μM .

An essential input towards further optimizing binding of the indazole moiety and exploring the unoccupied space of the substrate cavity region of hMAO-B was obtained by comparing the experimental data for the N1-methoxyethyl-substituted compound **15** and the docking experiments of **12a** and **13a** (Table 3). We esteem these findings to be crucial for future MAO-B inhibitor design, especially considering the optimal substituent length of four atoms and the type of functional groups needed. Docking studies and a subsequent HYDE analysis of all target structures are in line with a proposal of a non-covalent binding mode to human MAO-B, typically estimated for reversible inhibitors and experimentally confirmed for safinamide and the indazole derivatives **9** and **12a** [30–32].

2.4.2. Docking of compounds **12b** and **13b** into human MAO-A: applicability test in re-docking harmine

As a precaution it should be noted that the unavailability of a MAO-A co-crystal structure with a comparably large ligand leaves uncertainties for this molecular modeling proposal that uses fixed protein heavy atom positions. Regrettably, we could not get hold of the simulated receptor structure of

the human MAO-A enzyme alone; to the best of our knowledge it has not yet been disclosed [50]. We therefore used the co-crystal structure available in the PDB that had been co-crystallized with harmine as a small molecule ligand in the binding pocket [40]. Harmine, as crystallized at 2.2 Å resolution in the PDB (2Z5X) is an only 212 Da compound – as opposed to the much larger compounds **12b** (320 Da) and **13b** (304 Da); the same applies to the topological surface area (TPSA) of 37.9 Å³ compared to approximately 47 Å³ for **12b** and **13b**, respectively. In light of this, we expected a necessary removal of water in the vicinity to accommodate the larger ligands **12b** and **13b**. Analyzing the pocket, it can be noted that harmine in 2Z5X is surrounded by several water molecules, notably: (i) HOH726: situated between the FAD cofactor and acting as a donor to the pyridyl-N acceptor of harmine (the "left" water), (ii) HOH746: located below the pocket, forming a bridging interaction between harmine's protonated indole-N and ASN181 (the "low" water) and (iii) HOH766: found on the right side of harmine's methoxy-function, interacting with ALA111 (the "right" water). To re-dock harmine with LeadIT, we left all these water molecules present; subsequent SeeSAR HYDE scoring succeeded with a slight underestimation of the score (for more details, see Supporting Information). As the authors describe in the X-ray analysis of 2Z5X [40] the region of residues 109–112 (that is not too far from the methoxy-function of harmine) seems to be associated with flexibility, and potentially even a gating function so that this area may not be as preserved as assumed by our computations. Having obtained confidence in the applied methods, we conducted the same computational procedure for **12b** and **13b**. The above-mentioned explicit removal of the "left" water molecules created the necessary space, and subsequent docking embedded in SeeSAR retrieved well-scored poses for both compounds with torsions that are in statistically often-observed ranges (green colors on non-terminal X-H rotatable bonds in SeeSAR). We would like to briefly discuss compounds **12b** and **13b** in comparing their proposed binding modes to the one of harmine (Fig. 10).

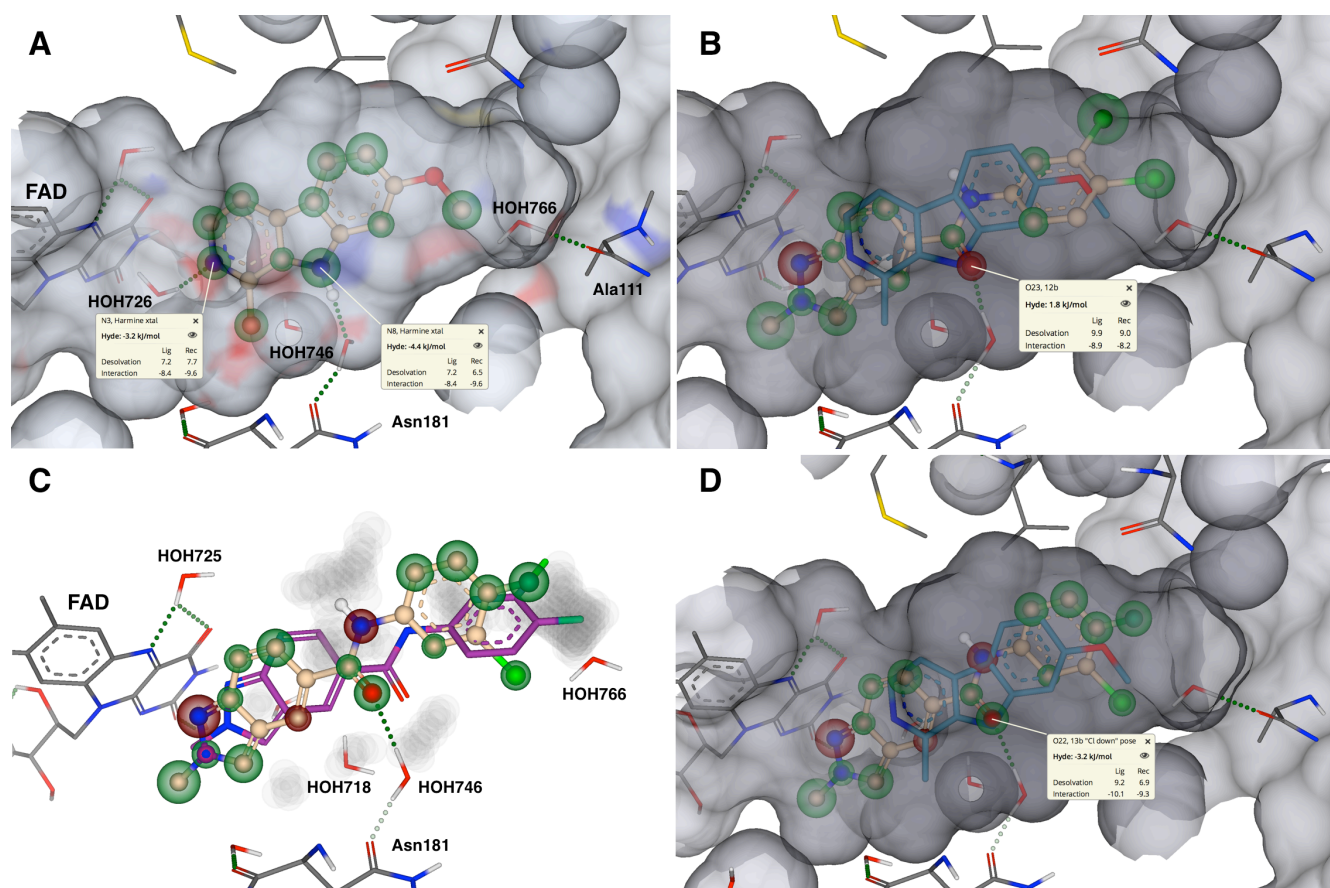


Fig. 10. SeeSAR visualization of binding in human MAO-A (PDB: 2Z5X): Protein residues except ASN181 and ALA111 have been omitted for clearness. Water molecules that are computed as relevant are automatically oriented in SeeSAR and have been labeled (HOH718, 725, 726, 746 and 766). HYDE corona coloring of the atomic affinity contributions: green = good, red = bad for affinity. (A): Binding of harmine in its X-ray structure. (B): Computed binding proposals for compound **12b** with harmine in blue. (C): The two most sensible pose proposals for **13b**, the more favored "Cl down" pose in off-white, the less favored "Cl up" pose in violet. (D): **13b** with harmine in blue; Panel D nicely shows the exact overlay of both the **13b** amide-O at the very position of harmine's indoyl-N.

In the template co-crystal structure shown in Fig. 10, harmine's indole nitrogen is bound to the water molecule number 746 (the "low" water), and the interaction is considered very favorable by the HYDE estimation (-4.4 kJ/mol, i.e., more than one order of K_i as a contribution). It is in fact one of the only two *directed* interactions between harmine and the protein that we detect – both being bridged to water molecules; the second one is between the pyridyl-N and HOH726 (the "left" water), contributing with -3.2 kJ/mol. All other relevant energetic contributions are non-directed and (de-)hydration/(de-)solvation-driven.

Now considering the dockings for compounds **12b** and **13b**, we propose that the central "fixation" by water 746 (the "low" water) is formed for both new compounds, however the higher space requirements of the two chlorine atoms in **12b** make the carboxamide oxygen move slightly unfavorably. The perfect geometry with the "low" water lone pairs as observed with harmine cannot be kept up anymore, and the desolvation penalties from the ligand side are no longer overcompensated by the gain in interaction energy; a small, yet unfavorable red HYDE "corona" visualization is the consequence (Fig. 10B).

As shown in Fig. 10C, docking of **13b** and subsequent scoring reveal two essentially equally scored poses: "Cl up" (violet) and "Cl down" (off-white). Our modeling cannot reliably predict which one is the more appropriate/correct one. Both exhibit torsions that are predominant in statistics analyses obtained from the CSD, as can be deduced from the green color on the bonds in Fig. 10C. However, the "Cl down" conformation exhibits the acceptor function (carbonyl oxygen) at exactly that position where the central acceptor-N of harmine residues – forming a favorable H-bond as in harmine with HOH746 (Fig. 10D). In addition, the "tightness of fit", i.e., the space filling is also optimized which can be deduced from the little amount of the "*explorability fog*" that SeeSAR displays around the molecule compared to the alternative pose proposal (fog not shown). In any of the dockings, the N1 position is close to the FAD cofactor and appears not to contribute favorably to the overall binding affinity. The 3-chloro-4-fluoro-phenyl substitution pattern in **13b** leaves a little more "leeway" for the ligand to still gain a favorable, central water 746 interaction while still realizing a planar amide connection and a clash-free filling of the pocket formed by residues 208–210, 223, and 235.

In addition, the modeling computations suggest that the central bridged water binding with its strong associated angular dependency induces geometric positioning of the ligands. The rest seems to be mainly desolvation-driven and the central part of the molecules is constrained to stay planar by the amide torsional barrier. A rotation about the indazole and carbonyl C-CO bond was sterically not tolerated: The N2-methyl substituent could not be placed without producing clash with the FAD.

Compared to harmine, whose crystal structure exhibits a hydrophobic carbon (the one next to the pyridyl N-atom) in the vicinity favorably positioned into the space between FAD's aromatic system and TYR407, the new ligands appear with their N1 atom in the corresponding area – entailing a potential loss of binding energy from desolvation. SeeSAR computed the trends correctly but underestimates the overall binding energy, which may give rise to the assumption that protein movements alleviate this situation in reality.

Summarizing the molecular modeling experiments, we applied a new approach combining both single X-ray and HYDE analyses in the SeeSAR molecular design platform to rapidly evaluate the therapeutic potential of new N1-alkylated indazole-5-carboxamide compounds **12a–15** and their N2-methyl analogs **12b–14b** as selective MAO-B and dual MAO-A/B inhibitors, respectively. A novel free energy approximation concept "HYDE" was used to help understanding activity and selectivity differences in N1- and N2-methylated regioisomers (compounds of subclasses II and III) by visualization and quantification of effects of (de-)hydration and hydrogen bonds.

2.5. Evaluation of tautomers of **11**

In order to get an insight into the possible tautomer formation and to confirm the accuracy of the docking experiments of indazole-5-carboxamide MAO inhibitors, the *N*-unsubstituted precursor *N*-(3,4-difluorophenyl)-1*H*-indazole-5-carboxamide (**11**) was selected for the analysis of a possible tautomerism of the indazole moiety and carboxamide linker by means of photophysical experiments and quantum-chemical calculations.

Electronic absorption and fluorescence excitation-emission spectra of compounds **11** were measured in anhydrous DMSO, acetonitrile, methanol, and methanol–water mixture (1:1) at a concentration of 0.5 mM and the results are summarized in Table 4. The absorption maxima (λ_{abs}) lie in the range of 275–283 nm. The emission maxima (λ_{em}) of **11** were found to be in the range of 326–376 nm at an excitation of 282 nm (DMSO and ACN) and 288 nm (methanol and methanol–water 1:1).

Compound **11** showed moderate to high Stokes shifts ($\Delta\lambda$, 51–94 nm) and the highest $\Delta\lambda$ value of 94 nm was observed in methanol–water mixture (1:1), as expected. The UV-Vis and fluorescence spectra showed that no solvent dependent spectral changes occurred, suggesting that under these experimental conditions **11** exists in its stable tautomeric 1*H*-indazole form (for details, see Fig. S8, Supporting Information). In the case of a 2*H*- or 3*H*-tautomer formation, spectral changes would be observed for both compounds in methanol–water mixture (1:1), where hydrogen bond interactions take place. These results were confirmed by quantum-chemical density functional calculations performed with the uncharged possible tautomeric forms of **11** [51]. The possible 1*H*- and 2*H*-indazole and keto-enol tautomeric forms of **11** are sketched in Fig. S9, and the relative energies are collected in Tables S14 and S15, respectively.

Table 4 Photophysical data of compound **11** (0.5 mM) in different solvents.

Compd.	DMSO				ACN				MeOH				MeOH–Water (1:1)			
	λ_{abs}^a	λ_{em}^a	$\Delta\lambda^a$	ϵ^b	λ_{abs}^a	λ_{em}^a	$\Delta\lambda^a$	ϵ^b	λ_{abs}^a	λ_{em}^a	$\Delta\lambda^a$	ϵ^b	λ_{abs}^a	λ_{em}^a	$\Delta\lambda^a$	ϵ^b
11	283	339	56	1371	275	326	51	2104	281	351	70	1685	282	376	94	1168

^a Unit: nm. ^b Unit: M⁻¹cm⁻¹.

The results arising from the calculations suggested that there is no tautomeric equilibrium in **11**. The compound exists as a stable tautomer (confirmed by X-ray and NMR analysis), strongly stabilized with respect to its next best stable form **b**. Each of the tautomers of **11** exists as a mixture of commensurable amounts of isomers, arising as a consequence of rotation around C-CO and NH-C single bonds. Their absorption spectra are practically identical and it is impossible to identify the individual tautomers by UV-Vis spectroscopy. There is no solvent effect on the tautomerism leading to specific interaction that can stabilize one or another tautomer. The absorption spectra's shape in **11** remains if the solvent is changed (starting from acetonitrile and going to methanol and then to DMSO and water), even in solvents with strong proton acceptor abilities like DMSO. Most probably the specific interactions are not strong enough to stabilize the **b** tautomer. The long-wavelength absorption

bands of **11a** are almost identical for differing solvents. The same is computed by the calculations. The theoretical values for λ_{\max} are lower compared to the experiment, but this is a systematical deviation caused by the use of the M06-2X density functional calculations (underestimation of the band positions) [51]. Comparing the X-ray structure of **11** with the calculations, the crystal structure is presented in **11a'**, but the energy difference with the calculated conformation **11a** is in the expected range of error (0.20 kcal/mol).

Taking into account the free rotation, it can be summarized that both theory and experiment coincide. From the X-ray data two details can be seen – there is an interaction between NH and C=O from two neighboring molecules which causes steric hindrance between F-containing phenyl rings and hence non-planarity (they are planar according to the calculations); this interaction is perhaps the reason for the orientation of the F-atoms (larger than hydrogens) providing packing in the solid state as **11a'**. Furthermore, our results indicate that the high inhibitory potency and selectivity of the *N*-unsubstituted indazole-5-carboxamide MAO-B inhibitors **9–11** relate to their *1H*-indazole tautomeric form, which appears to be favorable under physiological conditions ($\text{pH} \leq 7.4$). Moreover, we did not observe any evidence (neither from the photophysical studies nor via theoretical calculations) for not even a partly formation of a mixture of tautomeric forms of **11** (e.g., indazole and keto tautomeric forms **11a** and **11a'**, respectively) under these experimental conditions (cp. Table S15). As demonstrated by the chemical experiments, the *N*-unsubstituted indazole-5-carboxamides **9–11** can be easily deprotonated under basic conditions ($\text{pH} > 8$) leading to an *in situ* formation of a mixture of both indazole tautomeric forms **a** and **b** and, therefore, towards N1- and N2-alkylated products **12–14** (cf. Table 1). Based on quantum-chemical calculations, it can be further concluded that indazole-5-carboxamides exist in their more favorable keto tautomeric form of the carboxamide linker, which seems to be crucial for inhibitory activity through formation of hydrogen bonds with the water molecules within the active site of the human MAO A and B enzymes. These experimental observations give further support to the results obtained from the docking experiments in this work.

2.6. Profiling of physicochemical properties

2.6.1. Evaluation of drug-likeness

In the present study, the aim of optimizing the physicochemical parameters of *N*-unsubstituted indazole-5-carboxamides (subclass I) represented by a lead compound **11** while maintaining MAO inhibitory activity was carried out by an alkylation either at the N1- or N2-position of the indazole moiety, respectively. Based on their remarkable specific MAO-B or dual MAO-A/B inhibitory activity, compound **11** and *N*-methylated derivatives **12a,b–13a,b**, respectively, were selected for further evaluation of drug-likeness. For this purpose, relevant ADME properties (absorption, distribution, metabolism, and excretion) of the selected compounds were determined and calculated with main focus on the specific requirements for early stage in CNS drug development.

To access the drug-like properties of indazole-5-carboxamides, we determined the kinetic aqueous solubility (60 mM phosphate buffer at RT) and the distribution coefficients (logD, *n*-octanol-buffer 60 mM at RT) of the selected compounds at physiologically relevant pH values, namely pH 2.0, pH 5.5, and pH 7.4 (for details, see Tables S16 and S17, Figures S10–S13, Supporting Information). Measured aqueous solubility (expressed as logS_{7.4}) and logD_{7.4} values are presented in Table 5. Additionally, we calculated several physicochemical parameters, including hydrogen bond acceptors and donors (HBA and HBD) counts, topological surface area (*t*PSA) [52], blood (plasma)-brain partition coefficient (logBB) [53], and ligand-lipophilicity efficiency (LLE) [54,55] of the indicated compounds and compared them to the reference MAO-A and MAO-B reversible inhibitors moclobemide and safinamide, respectively.

In the kinetic solubility assessments, we considered compounds with a solubility value of <10 μM (logS < -5) to be highly insoluble, between 10 and 100 μM (-5 < logS < -4) as partially soluble and >100 μM (logS > -4) to be highly soluble. In general, almost all tested compounds show pH-independent solubility, indicating that these compounds will be uncharged in the physiological relevant pH range of 2.0–7.4. With the exception of **12a**, all of them show good to excellent aqueous solubility in

the whole investigated pH range, which is crucial for oral bioavailability of this class MAO inhibitors. We found that under these test conditions, especially a fluoro-substituent at the *para*-position of the phenyl ring and N1- over N2-methyl substitution of the indazole moiety has an impact on solubility. The most potent MAO-B inhibitor of all investigated compounds, compound **12a**, exhibiting an N1-methyl substituent and two chlorine atoms at the *meta*- and *para*-position of the phenyl ring, is the less soluble one. In contrast, the N2-methyl-substituted compound **13b**, bearing a fluorine atom in the *para*-phenyl position, exhibits the highest solubility ($\log S_{7.4} = -3.36$, 439 μM at pH 2.0, >420 μM at pH 5.5, and 441 μM at pH 7.4), being ~7-fold more soluble than its N1-methylated isomer **13a** ($\log S_{7.4} = -4.11$, 77 μM). On the other hand, the introduction in compound **12a** (3,4-Cl-Ph) of a fluorine atom at the *para*-position of the phenyl ring led to a 22-fold increase in solubility of **13a** (3-Cl, 4-F-Ph). Moreover, **13b** shows higher solubility than the standard MAO-B inhibitor safinamide (calcd. $\log S_{7.4} = -4.06$). In general, N2-methyl-substitution of the indazole moiety (compounds **12b** and **13b**) led to a significant increase of solubility at all three pH values when compared to their N1-methyl-substituted analogs (cf. **12a** and **13a**). Compared to **13b**, compounds **11**, **12b** and **13a** display partial solubility, however it is still high for predictive oral bioavailability ($\log S > -5$, >10 μM). The N1-methyl-substituted derivative **13a** demonstrates a different behavior compared to all other tested compounds; it shows a slight pH-dependent improvement in solubility (~58 μM at pH 2.0, 69 μM at 5.5, and >77 μM at pH 7.4).

Lipophilicity ($\log P$) is a key structural factor that affects high-level physicochemical and biological properties governing both pharmacokinetics and pharmacodynamics of drugs. Thus, the distribution coefficient ($\log D$) of compounds **11** and **12a–13a,b** provides a thermodynamic measure of their hydrophilicity-lipophilicity balance. For an optimal gastrointestinal (GI) absorption by passive membrane permeability after oral administration, a $\log D$ value in the range of 1–3 would be preferable in order to ensure a good balance between permeability and solubility [56]. As was the case with the aqueous solubility, the $\log D$ values for all selected compounds are non-dependent on pH value of buffer used in this study, suggesting that indazole-5-carboxamides **11** and **12a,b–13a,b** exist in their neutral

forms across the pH range of 2.0–7.4. It can therefore be assumed that the logD values of these compounds are almost equal to their lipophilicity values in neutral form (at pH 2.0–7.4 $\log D \approx \log P$). Determined $\log D_{7.4}$ values for the majority of tested compounds are in the ideal range of less or about 3, being in the same or similar range as the reference CNS drugs safinamide and moclobemide (Table 5). Furthermore, we observed a good correlation between the measured logD values and the kinetic aqueous solubility data for the most compounds. Apparently, compound **12a** that is the most potent, however less soluble MAO-B inhibitor, shows logD values that exceed the above-mentioned range slightly ($\log D_{2.0} = 3.09$, $\log D_{5.5} = 3.35$ and $\log D_{7.4} = 3.24$). This complies with the importance of hydrophobic effect contributions to the overall binding energy (cp. Modeling Section above). Surprisingly, the most soluble N2-methylated derivative **13b** exhibits a $\log D_{2.0}$ value of 3.24, which is comparable to the one observed for **12a**.

Overall, the physicochemical properties for the selected indazole-5-carboxamides are in the suggested limits for drug-likeness of CNS+ drugs ($MW \leq 400$, $HBA < 7$, $HBD < 3$, and $tPSA < 70 \text{ \AA}^2$) [52,56,57]. Compound **11** has lower molecular weight (MW) than the reference drug safinamide, similar to the one of moclobemide, whereas compounds **13a** and **13b** have MWs that are close to the one of safinamide. The $tPSA$ values for all selected compounds are in the range between 46.9 and 57.8 \AA^2 indicating that they are expected to be orally bioavailable and classified as “good” for brain penetration under the limit of 60 \AA^2 [52]. Therefore, these compounds may be considered as promising CNS drug candidates [55].

To predict the BBB permeability properties of selected compounds, we also calculated the blood(plasma)-brain partition coefficient ($\log BB$) [53]. Compounds with $\log BB < -1$ are poorly distributed to the brain [52]. All indazole-5-carboxamide derivatives in Table 7 show a $\log BB > -1$, indicating a possible BBB permeability. Moreover, compounds **12a** ($\log BB = 0.246$), **13a** ($\log BB = 0.216$), **12b** ($\log BB = 0.264$) and **13b** ($\log BB = 0.224$) exhibited higher $\log BB$ values than those of the reference drug safinamide ($\log BB = -0.083$).

Table 5 Drug-like properties of selected indazole-5-carboxamides and reference MAO inhibitors.

Compd.	R	R ¹	MW	pIC ₅₀	HBA ^a	HBD ^a	tPSA ^a	logBB ^a	logS _{7.4} ^b	logD _{7.4} ^c	LLE ^d
11	3,4-F	H	273.07	8.18	4	2	57.78	-0.002	-4.22	2.04	6.14
12a	3,4-Cl	Me	320.17	9.41	4	1	46.92	0.246	-5.45	3.24	6.17
12b	3,4-Cl	Me	320.17	8.84	4	1	46.92	0.264	-4.25	2.97	5.87
13a	3-Cl, 4-F	Me	303.72	9.18	4	1	46.92	0.216	-4.11	2.19	6.99
13b	3-Cl, 4-F	Me	303.72	8.09	4	1	46.92	0.224	-3.36	2.64	5.45
M	-	-	268.74	6.44 ^e	4	1	41.47	0.048	-1.83 ^a	1.41 ^a	5.03
SAF	-	-	302.34	8.29	4	1	64.68	-0.083	-4.06 ^a	2.89 ^a	5.40
^f CNS+			≤400	>8	<7	<3	<60–70	≥-1	≥-5.0	1–3	>5

MW, molecular weight. HBA, number of hydrogen bond acceptors. HBD, number of hydrogen bond donors. tPSA, topological surface area (in Å²). M, Moclobemide. SAF, Safinamide. ^a Properties evaluated using the StarDrop module in SeeSAR 5.4, 2016 [43]. ^b LogS (in mol/L) at pH 7.4 in 60 mM phosphate buffer at RT. ^c Distribution coefficient at pH 7.4 in 60 mM phosphate buffer at RT. ^d LLE, ligand-lipophilicity efficiency = pIC₅₀ - logD_{7.4}. ^e pIC₅₀ human MAO-A. ^f Ref. [52,56–58]

The ligand-lipophilicity efficiency is a multiparameter score that is frequently used for evaluation of lipophilicity contribution to *in vitro* potency (pIC₅₀ or pK_i) [58]. All selected compounds possess a LLE score in the optimal range for drug candidates suitable for further *in vivo* evaluation (5 < LLE < 7). Again, compounds **11–13** show higher LLE values than the one of safinamide (LLE = 5.4).

To further assess the structure-properties relations (SPRs), we plotted molecular weight (MW) versus the logD_{7.4} values (Golden Triangle) [58] and the pIC₅₀ values (hMAO-B or hMAO-A) versus the logD_{7.4} values (LLE score) for all selected compounds as well as reference drugs moclobemide and safinamide (Fig. S14, see Supporting Information). From the Golden Triangle radar plot, it appears evident that all evaluated compounds exhibit or are predicted to have optimal drug-like properties suitable for good clearance and oral absorption [56]. Moreover, the compounds show excellent ligand-lipophilicity efficiency values (LLE > 5) and we therefore suggest they should be considered for further drug development [56].

2.6.2. Evaluation of *in vitro* BBB and GI permeability

A fine balance between oral bioavailability (solubility) and brain penetration (lipophilicity) is a major requirement for successful CNS drugs. One of the main goals of the current work is to investigate the blood-brain barrier (BBB) and gastrointestinal (GI) permeability within the series of *N*-methylated indazole-5-carboxamides with regard to their further development either as specific MAO-B or dual MAO-A/B inhibitors and radioligands. For the majority of CNS drugs, oral administration is the most preferred route of medication; drugs permeate both the GI tract (GIT) and the BB barrier mostly by transcellular passive diffusion. Poor solubility, which is associated with high lipophilicity, can be a limiting factor for GI absorption of compounds, thus reducing their oral bioavailability [59]. On the other hand, highly lipophilic compounds can penetrate through the BBB easily and reach the biological target at sufficiently high therapeutic concentrations [60]. Parallel artificial membrane permeability assay (PAMPA) is a widely used high-throughput test for transcellular passive permeability assessment [61] that allows a rapid and simple prediction of passive diffusion through different types of human barriers depending on the artificial lipid membrane that is applied [61–63].

Therefore, to examine whether the indazole-5-carboxamides **11** (subclass I) and **12a,b–13a,b** (subclass II and III) are able to pass through the GI tract and to penetrate into the brain, PAMPA-GI and PAMPA-BBB experiments were performed. In the PAMPA assays, we used verapamil as high permeability standard and theophylline as low permeability standard [61]. These commercial drugs were tested at three initial concentrations in PAMPA-BBB (50, 100, and 200 μM) and at 200 μM in the PAMPA-GI assay. The experimental permeability determined for verapamil and theophylline show a good agreement with the reported values, so it can be assumed that the assay conditions of both PAMPA experiments are reliable (for details, see Table S18 and Fig. S15–S18, Supporting Information). To achieve an accurate prediction of oral bioavailability, permeability in the PAMPA-GI assay was measured at three different pH values (2.0, 5.5 and 7.4) to mimic the physiological pH gradient of the GI tract [60]. In the PAMBA-BBB model, all compounds were assessed only at pH 7.4 that corresponds to the physiological pH in the blood compartment. The *in vitro* permeability (P_e) of investigated

compounds **11–13** and standard drugs across a L- α -phosphatidylcholine lipid membrane (for PAMPA-GIT) and a porcine brain lipid membrane extract (for PAMPA-BBB) was determined and is reported in Table 6.

Table 6 Permeability ($P_e \times 10^{-6}$ cm/s) in the PAMPA GI and BBB assays for compounds **11–13**.

Compd.	PAMPA-GI ^{a,b,c}			PAMPA-BBB ^{a,c}	Prediction of BBB permeation
	pH 2.0	pH 5.5	pH 7.4	pH 7.4	
11	≤ 0.59	≤ 0.59	≤ 0.59	8.15 ± 0.66	CNS±
12a	18.3 ± 1.68	16.8 ± 2.08	18.6 ± 2.50	22.3 ± 3.75	CNS+
12b	14.5 ± 0.80	16.1 ± 1.50	17.6 ± 1.37	29.0 ± 2.15	CNS+
13a	27.2 ± 0.47	29.5 ± 0.53	31.7 ± 1.16	37.6 ± 1.95	CNS+
13b	8.16 ± 0.21	9.11 ± 0.85	9.35 ± 0.37	17.2 ± 3.40	CNS+
Verapamil ^d	<0.59	<0.59	24.4 ± 1.36	34.9 ± 3.14	CNS+
Theophylline ^d	<0.59	<0.59	<0.59	≤ 0.59	CNS–

^a The values are the mean \pm SD of three independent experiments. ^b PAMPA-GI: pH value of 60 mM phosphate buffer. ^c 60 mM PB-EtOH (80:20) was used as solvent. ^d Measured at 200 μ M initial concentration CNS+: high BB permeation predicted, CNS±: uncertain BBB permeation predicted, CNS–: low BBB permeation predicted.

Permeability coefficients (P_e) of compounds were obtained from the respective concentrations determined at their specific λ_{\max} in both donor and acceptor compartments after incubation time of four hours. In our PAMPA assays and taking into account the structure-property relations (SPRs) obtained from the physicochemical studies, the permeabilities of compounds were ranked into two classes for simplification as follows: (i) high GI and BBB permeable compounds with $P_e > 10 \times 10^{-6}$ cm·s⁻¹ and (ii) low GI and BBB permeable compounds with $P_e < 10 \times 10^{-6}$ cm·s⁻¹. Similar classifications can also be found in the literature for the prediction of human intestinal absorption (HIA) [64] and BBB permeation, e.g., compounds classified by high (CNS+), uncertain (CNS±) and low (CNS–) permeability through the BB barrier [60]. The results for the PAMPA-GI assay show that the permeability of compounds **11** and **12a,b–13a,b** is independent of the pH value of buffer used in this study. This is no surprising when considering that these compounds are non-ionizable at the physiological pH range below 7.4. Compounds **12a**, **12b** and **13a** can be classified as highly permeable and should cross the GI tract by passive absorption, which is predictive for oral bioavailability. The opposite effect was observed for *N*-

unsubstituted indazole-5-carboxamide **11**; this compound could be classified as non-permeable, which does not undergo passive diffusion through the GIT. The N2-methylated derivative **13b**, that is the most (aqueous) soluble molecule (434 μM on average across the pH range 2.0–7.4) within all tested compounds, was predicted to be lowly GI permeable. As expected, the standard drug verapamil showed pH-dependent permeation along the GIT, while theophylline is non-permeable in the pH range 2.0–7.4.

On the basis of the PAMPA-BBB results, the N1-methylated indazole-5-carboxamides **12a** and **13a** (compounds of subclass II) and their N2-methylated analogues **12b** and **13b** (subclass III) can be classified as highly permeable under tested conditions. These compounds are predicted to be able to cross the BBB by passive permeation exhibiting P_e values that are comparable to the permeability of verapamil measured at different concentrations. Moreover, compound **13a** showed higher BBB permeability to that observed for verapamil at 200 μM initial concentration. In contrast, compound **11** exhibited the lowest BBB permeability of all compounds tested, although it can be classified as compound with a high BBB permeation ($P_e = 8.15 \times 10^{-6} \text{ cm}\cdot\text{s}^{-1}$) when compared to the well-established limit in the literature ($P_e > 4.0 \times 10^{-6} \text{ cm}\cdot\text{s}^{-1}$) [60]. In addition, the results obtained for theophylline were in accordance with its different mechanism of transcellular transport [60].

Overall, the PAMPA GI and BBB results reproduced the SARs and SPRs obtained from the evaluation of the biological and drug-like properties of the selected compounds. Depending on the substitution pattern of the indazole moiety, significant differences in permeability in the *in vitro* GI and BBB models between the *N*-unsubstituted indazole-5-carboxamide **11** (subclass I) and the N1-/N2-methylated derivatives **12a,b–13a,b** (subclass II and III) could be observed (Fig. 11).

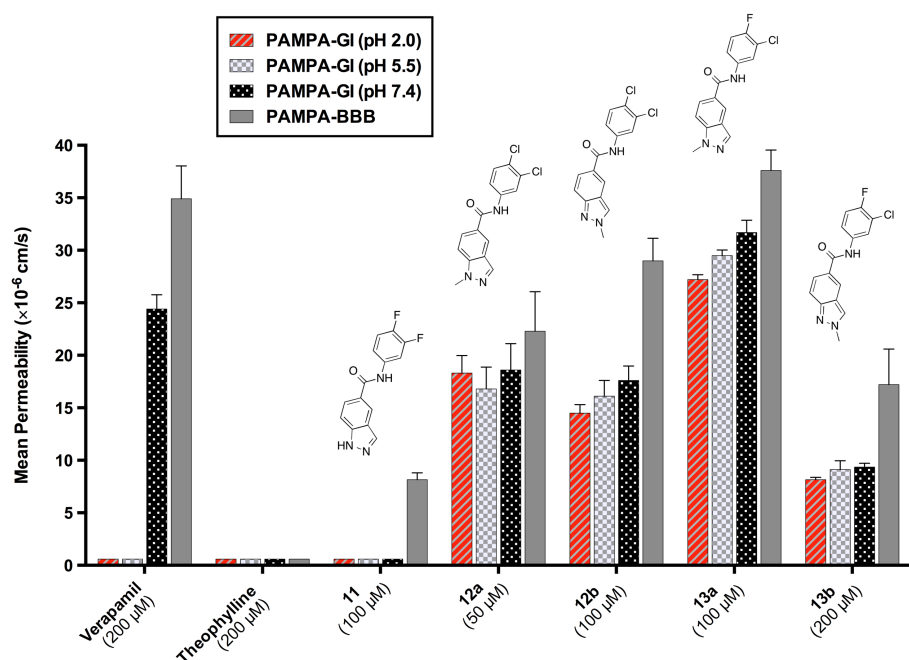


Fig. 11. Distribution of GI and BBB mean permeability of standard drugs and compounds **11–13** measured in the PAMPA assay. Each data point represents the mean \pm SD (N = 3). The initial test concentrations are indicated.

While **11** is not GI permeable and, according to our ranking, with low predicted BBB permeability (CNS \pm), compounds of subclass II and III were found to be GI permeable with predictive oral absorption and highly CNS penetrant (CNS+) in our PAMPA-BBB assay. Seeing that all these indazole-5-carboxamides exhibit pH-*independent* $\log D_{pH(x)}$ values (within the optimal range of 2–4 for CNS drugs across the physiologically relevant pH range of less than 7.4), this raises the responsibility of their structural properties for their good GI absorption (solubility) and BBB permeability (lipophilicity). Thus, the N1- and N2-methylated derivatives of subclass II and III are predicted to reach the therapeutic target in the human brain through passive diffusion, whereas the *N*-unsubstituted compound **11** (subclass I) does not cross the GI tract by passive transport. We refrained from any further assumptions for **11** to not include even additional studies (e.g., Caco-2). A good correlation between aqueous solubility data and permeability (GI and BBB) could be observed for compound **13b**. Summarizing our

results from the GI and BBB PAMPA studies and the ADME analyses, the *N*-methylated compounds **12–13** can be classified as highly permeable with well-balanced solubility-lipophilicity properties [65].

3. Discussion of the SAR and SSR studies

Considering the hydrophobic character of the active site of the human MAO-B and the binding interactions observed for standard inhibitors [38,40,41], the combination of small lipophilic substituents at positions 3 and 4 of the phenyl ring with a methyl or a methoxyethyl group at the indazole N1 position is well-tolerated by hMAO-B resulting in best-in-class MAO-B inhibitors so far (indazole-5-carboxamides subclass II). All compounds were found to be highly potent inhibitors of rat and human MAO-B without noticeable inhibition of rat and human MAO-A isoform. The majority of them are significantly more potent (3–13-fold) and selective for MAO-B (up to 5-fold) than the current reversible standard MAO-B inhibitor safinamide. Biological data suggest that N1-methylated indazole-5-carboxamides with a 3,4-dichlorophenyl (**12a**) or a 3-chloro-4-fluorophenyl residue (**13a**) represent MAO-B inhibitors with IC₅₀ values in the picomolar range. The compounds showed >13-fold (**12a**) and 8-fold (**13a**) increase in inhibitory potency when compared to safinamide. In the series of N2-methyl-substituted indazole-5-carboxamides (subclass III), dual active MAO A and B inhibitors were identified. For these, we observed similar SARs (e.g., dependency on the lipophilic character of the 3,4-disubstituted phenyl ring) but different SSRs compared to their N1-methyl analogs. The most potent dual acting inhibitor was compound **12b**, bearing a 3,4-dichlorophenyl ring. It inhibits human MAO-B in the subnanomolar range and shows a 4-fold increase in inhibitory potency in comparison to those observed for safinamide, and a similar potency as the standard MAO-A inhibitor moclobemide. These results indicate that the indazole NH is not required as a hydrogen bond donor, and the indazole nitrogen atoms N1 and N2 may act as electron donors within the binding pocket of human MAO A and B. Thus, the optimized pharmacophore features of the compounds under study were a lipophilic 3,4-dihalophenyl ring (Ph), a polar carboxamide linker serving as hydrogen bonding domain (HBD) with hybrid feature, providing an H-bond acceptor (the carbonyl oxygen), and a N1- or N2-methyl-substituted 5-indazole

core with combined electron donating (ED) and hydrophobic properties (Fig. 12). Detailed analyses of the distances between the centroids of the pharmacophore groups (phenyl ring, carboxamide function and the indazole nitrogen atoms) suggest that the optimal length of the spacer is characterized by two atoms between the lipophilic phenyl part and the hydrophobic electron donating unit in the indazole-5-carboxamide scaffold. The distances in compounds **12a,b** and **13a,b** within the active site of human MAO-B are similar to those in **12b** and **13b** as docked into the human MAO-A enzyme, except for Ph-ED, which is longer (Table 7). An extension and/or an inversion of the amide linker would not only lead to a significant decrease of MAO activity in general [30], but also to a rigorous disturbance of the hydrophilic-lipophilic balance of the *N*-substituted indazole-5-carboxamide derivatives (compounds of subclass II and III).

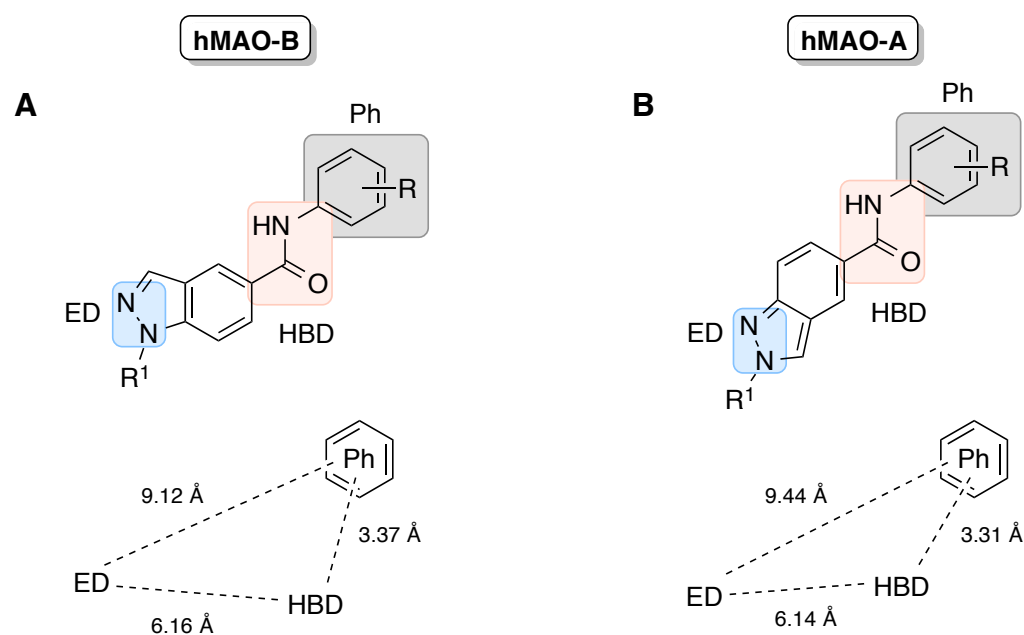


Fig. 12. Distances in triangle pharmacophores for compounds **13a** and **13b**; values were obtained from the best SeeSAR docking conformations within the human MAO-B (A) and human MAO-A (B).

Table 7 Measured distances (in Å) between pharmacophoric features in compounds **12a,b** and **13a,b**.

Compd.	MAO isoform	Ph-Ring...ED	HBD...ED	Ph-Ring...HBD
12a	hMAO-B	9.023	6.153	3.395
12b	hMAO-B	9.152	6.116	3.389

	hMAO-A	9.294	6.113	3.250
13a	hMAO-B	9.117	6.161	3.374
13b	hMAO-B	9.077	6.110	3.394
	hMAO-A	9.435	6.138	3.308

ED, electron donor N1 or N2 atom of the indazole moiety. HBD, hydrogen bonding domain of the carboxamide linkage.

SARs and SSRs show that (i) the MAO-B inhibitory potency of *N*-alkylated indazole-5-carboxamides strongly depended on the indazole N1-substitution in combination with a 3,4-dihalophenyl ring, (ii) both MAO-A inhibitory activity and the selectivity for hMAO-B over hMAO-A are affected by the substitution of the indazole N2 position, and (iii) an extension of the alkyl substituents either in the N1 or N2 position of the indazole moiety up to four atoms is well tolerated by hMAO-B enzyme, but not by its hMAO-A isoform.

4. Conclusion

In summary, we have investigated several pharmacological and physicochemical issues of new, structurally optimized *N*-alkylated indazole-5-carboxamide derivatives such as MAO A and B inhibition, the GI absorption, the BBB penetration, aqueous solubility, and logD values as important parameters of CNS active drugs. SAR and SSR analysis have led to the identification of remarkably potent, selective MAO-B (N1-alkyl-substituted compounds of subclass II) or dual active MAO-A/B (N2-methylated compounds of subclass III) inhibitors with subnanomolar potency. To find a plausible explanation for their high MAO-B affinity and the observed regioisomeric-based differences in selectivity, docking experiments were performed using a well-validated modeling platform utilizing the availability of single X-ray structures of selected compounds **9**, **11**, **12a**, and **13a**. Furthermore, we used the novel free energy approximation concept "HYDE" for estimation, visualization, and quantification of effects of (de)hydration and hydrogen bonding. We also investigated the possible tautomers of the *N*-unsusbstituted indazole-5-carboxamide precursor **11** (a subclass I compound) by means of photophysical experiments and quantum chemical calculations of its neutral and ionized forms in different solvents.

The results suggest that indazole-5-carboxamides exist in their more favorable keto form of the carboxamide linker and virtually stable 1*H*-indazole tautomeric form of the *N*-unsubstituted indazole unit. Moreover, we evaluated the drug-like and *in vitro* ADME properties of compounds **11–13**. Our results show that in general all investigated *N*-methylated indazole-5-carboxamide derivatives exhibit the suitable drug-like properties required for CNS drugs, and they are predicted to be highly GI and BBB permeable, as measured by *in vitro* PAMPA-GI and -BBB assays. All these compounds contain common pharmacophoric features contributing to their good solubility-lipophilicity balance. Thus, compounds **13a** and **13b** can be highlighted as selective MAO-B and dual MAO-A/B inhibitors, respectively, because of their predicted high oral absorption and brain penetration, combined with well-optimized drug-like and physicochemical properties (aqueous solubility, logD = 2–3, MW = 303 Da, LLE > 5.45), which support the potential of these compounds as promising drug and radioligand candidates, including diagnostics for positron emission tomography (PET), e.g., for the treatment and diagnosis of PD, possibly AD and other CNS diseases. Further efforts will be focused on specific structural exploration of these substance classes, in particular by introducing of different alkyl substituents in the indazole moiety, as well as investigation the compounds' metabolism and toxicity and to study the new MAO inhibitors in relevant animal models.

5. Experimental section

5.1. Chemistry

5.1.1. General methods

All commercially available anhydrous solvents, reagents, starting materials and reference compounds were obtained from various suppliers and used without further purification. Commercially available 1*H*-indazole-5-carboxylic acid (**1**, Aldrich) was used as starting material for the preparation of the *N*-alkylated carboxylic acid **7**. Dry *N,N*-dimethylformamide (DMF, 99.8% extra dry over molecular sieves, AcroSeal, Acros) was used throughout the synthesis. Ampuwa water-for-injection (WFI, Fresenius Kabi) was applied for preparation of single crystals suitable for X-ray analysis. Reactions were routinely monitored by thin layer chromatography (TLC) on pre-coated Merck 60 F₂₅₄ silica gel plates and visualized using UV light (254 nm light source). Preparative column chromatography was performed on Acros Organics silica gel 60Å (0.060–0.200 mm). The organic layer obtained after extraction from aqueous phases was dried over anhydrous sodium sulfate. Solvents were removed *in vacuo* on a Büchi Rotavapor R-100/R-300. Mass spectra were recorded on an API 2000 mass spectrometer (electron spray ion source ESI, Applied Biosystems) coupled with an Agilent 1100 HPLC system as described in the Supporting Information. Purification by RP-HPLC of the final products was performed on a Knauer Advanced Scientific Instruments HPLC system coupled to a PDA-based S2600 UV diode array detector (DAD). The purity of the compounds was determined by HPLC-UV obtained on a LC-MS instrument (Applied Biosystems API 2000 LC-MS/MS, HPLC Agilent 1100). All tested compounds possessed a purity of not less than 95%. ¹H and ¹³C NMR spectral data were obtained from a Bruker Avance 500 MHz NMR spectrometer. The ¹H and ¹³C NMR spectra were recorded at room temperature (303 K) using DMSO-*d*₆ as the solvent. Chemical shifts (δ) are reported in parts per million (ppm) relative to the residual solvent peak in the corresponding spectra: DMSO-*d*₆ δ 2.50 (¹H) and 39.51 (¹³C). Coupling constants *J* are given in Hertz (Hz), and spin multiplicities are given as singlet (s), broad

singlet (br s), doublet (d), doublet of doublets (dd), doublet of doublets of doublets (ddd), triplet (t), doublet of triplets (dt), quartet (q), and multiplet (m). Melting points are uncorrected and were determined on a Büchi Melting Point B-545 apparatus using open capillary tubes. The experimental procedure and spectroscopic analysis for the carboxylic acid **7** are provided in the Supporting Information. The indazole-5-carboxamide derivatives **8–12** were prepared as described for compound **15**. The analytical data of **8–12** are reported previously [31]. Compounds **12a** and **12b** were prepared using revised procedures, and for these, all analytical data is reported in the Experimental Section.

5.1.2. General procedure for the preparation of *N*-methylated compounds **12a,b–14a,b**

To a solution of the corresponding indazole-5-carboxamide **8–11** (1.0 equiv) and potassium carbonate (1.25 equiv) in DMF (6.0–8.0 mL/mmol; extra dry over molecular sieves, 99.8%, Acros) MMS (1.6–1.7 equiv) was added. The mixture was stirred at room temperature until completed conversion could be detected by TLC (mobile phase: CH₂Cl₂/MeOH 9/1 v/v), hydrolyzed with water (20 mL/mmol), and acidified with hydrochloric acid (2*N*, 2.0 mL/mmol). The formed precipitate was filtered under reduced pressure, washed three times with water (10 mL), and dried at 70 °C. The crude N1/N2-regioisomer mixture was separated by C18 reversed phase HPLC as described below.

5.1.2.1. *N*-(3,4-dichlorophenyl)-1-methyl-1*H*-indazole-5-carboxamide (**12a**) [31]

Purification was performed following RP-HPLC method 1 to afford **12a** as a white crystalline solid (42 mg, 53%); mp 193.2–194.3°C. ¹H NMR (500 MHz, DMSO-*d*₆) δ = 4.09 (s, 3H, N1Me), 7.61 (d, *J* = 8.82 Hz, 1H, Ph), 7.76 (d, *J* = 8.20 Hz, 1H, Ph), 7.78 (dd, *J* = 2.21 / 8.83 Hz, 1H, Ph), 7.98 (dd, *J* = 1.57 / 8.82 Hz, 1H, Ph), 8.18 (d, *J* = 2.52 Hz, 1H, Ph), 8.24 (d, *J* = 0.63 Hz, 1H, ind-het), 8.46 (dd, *J* = 0.63 / 1.57 Hz, 1H, Ph), 10.49 (s, 1H, -CONH-). ¹³C NMR (125 MHz, DMSO-*d*₆) δ = 35.7 (N1Me), 109.8, 120.3, 121.5, 121.9, 123.0, 125.0, 125.6, 126.7, 130.7, 131.0, 134.2, 139.7, 140.9, 166.1. ESI-MS (*m/z*): calcd. for C₁₅H₁₁Cl₂N₃O: 319.028; found 318.052 [M – H][–], 320.143 [M + H]⁺.

5.1.2.2. *N*-(3,4-dichlorophenyl)-2-methyl-2*H*-indazole-5-carboxamide (**12b**) [31]

Purification was performed following RP-HPLC method 1 to afford **12b** as a white solid (15 mg, 18%); mp 180.7–181.6°C. ¹H NMR (500 MHz, DMSO-*d*₆) δ = 4.23 (s, 3H, N2Me), 7.60 (d, *J* = 8.82 Hz, 1H, Ph), 7.68 (dt, *J* = 0.95/8.82 Hz, 1H, Ph), 7.75 (s, 1H, Ph), 7.76 (dd, *J* = 2.21/8.83 Hz, 1H, Ph), 8.16 (d, *J* = 0.63 Hz, 1H, Ph), 8.44 (dd, *J* = 0.94/1.89 Hz, 1H, Ph), 8.58 (s, 1H, ind-het), 10.45 (s, 1H, -CONH-). ¹³C NMR (125 MHz, DMSO-*d*₆) δ = 48.8 (N2Me), 116.9, 120.4, 120.9, 121.5, 122.4, 124.6, 125.0, 127.1, 127.2, 130.7, 131.0, 139.8, 149.1, 166.4; ESI-MS (*m/z*): calcd. for C₁₅H₁₁Cl₂N₃O: 319.028; found 318.043 [M – H][–], 320.132 [M + H]⁺.

5.1.2.3. *N*-(3-chloro-4-fluorophenyl)-1-methyl-1*H*-indazole-5-carboxamide (**13a**)

Purification according to RP-HPLC method 2 yielded **13a** as a white solid (35 mg, 52%); mp 171.4–172.4°C. ¹H NMR (500 MHz, DMSO-*d*₆) δ = 4.09 (s, 3H, N1Me), 7.41 (t, *J* = 9.14 Hz, 1H, Ph), 7.74 (ddd, *J* = 2.83/4.41/8.82 Hz, 1H, Ph), 7.76 (d, *J* = 8.83 Hz, 1H, Ph), 7.98 (dd, *J* = 1.89/8.83 Hz, 1H, Ph), 8.10 (dd, *J* = 2.5/6.94 Hz, 1H, Ph), 8.24 (d, *J* = 0.95 Hz, 1H, ind-het), 8.46 (q, *J* = 0.94 Hz, 1H, Ph), 10.42 (s, 1H, -CONH-). ¹³C NMR (125 MHz, DMSO-*d*₆) δ = 35.7 (N1Me), 109.8, 116.9 (d, *J* = 21.6 Hz), 119.1 (d, *J* = 18.2 Hz), 120.7 (d, *J* = 6.73 Hz), 121.7, 121.8, 123.1, 125.6, 126.9, 134.1, 136.8 (d, *J* = 2.99 Hz), 140.9, 153.4 (d, *J* = 242.84 Hz), 165.9. ESI-MS (*m/z*): calcd. for C₁₅H₁₁ClFN₃O: 303.057; found 302.062 [M – H][–], 304.124 [M + H]⁺.

5.1.2.4. *N*-(3-chloro-4-fluorophenyl)-2-methyl-2*H*-indazole-5-carboxamide (**13b**)

Purification according to RP-HPLC method 2 yielded **13b** as a white solid (13 mg, 20%); mp 187.8–188.1°C. ¹H NMR (500 MHz, DMSO-*d*₆) δ = 4.21 (s, 3H, N2Me), 7.40 (t, *J* = 9.14 Hz, 1H, Ph), 7.68 (td, *J* = 0.94/9.14 Hz, 1H, Ph), 7.74 (ddd, *J* = 2.84/4.41/9.14 Hz, 1H, Ph), 7.77 (dd, *J* = 1.89/9.14 Hz, 1H, Ph), 8.10 (dd, *J* = 2.52/6.93 Hz, 1H, Ph), 8.44 (q, *J* = 0.95 Hz, 1H, Ph), 8.59 (s, 1H, ind-het), 10.37 (s, 1H, -CONH-). ¹³C NMR (125 MHz, DMSO-*d*₆) δ = 40.4 (N2Me), 116.8, 116.9 (d, *J* = 21.7 Hz), 119.1 (d, *J* = 18.2 Hz), 120.6 (d, *J* = 6.98 Hz), 120.9, 121.7, 122.2, 124.5, 127.0, 127.2, 136.8 (d, *J*

= 2.99 Hz), 149.0, 153.3 (d, $J = 242.84$ Hz), 166.2. ESI-MS (m/z): calcd. for $C_{15}H_{11}ClFN_3O$: 303.057; found 302.063 $[M - H]^-$, 304.122 $[M + H]^+$.

5.1.2.5. *N*-(3,4-difluorophenyl)-1-methyl-1*H*-indazole-5-carboxamide (**14a**)

Purification according to RP-HPLC method 3 yielded **14a** as a white solid (37 mg, 54%); mp 172.4–172.6°C. 1H NMR (500 MHz, DMSO- d_6) $\delta = 4.09$ (s, 3H, NMe), 7.41 (q, $J = 10.72$ Hz, 1H, Ph), 7.54–7.59 (m, 1H, Ph), 7.75 (d, $J = 8.83$ Hz, 1H, Ph), 7.95 (dd, $J = 2.52/7.57$ Hz, 1H, Ph), 7.98 (dd, $J = 1.58/8.83$ Hz, 1H, Ph), 8.24 (d, $J = 0.63$ Hz, 1H, ind-het), 8.45 (q, $J = 0.95$ Hz, 1H, Ph), 10.43 (s, 1H, -CONH-). ^{13}C NMR (125 MHz, DMSO- d_6) $\delta = 35.7$ (N1Me), 109.3 (d, $J = 21.7$ Hz), 109.8, 116.6 (q, $J = 3.24$ Hz), 117.4 (d, $J = 17.7$ Hz), 121.7, 123.1, 125.6, 126.9, 134.1, 136.6 (dd, $J = 2.74/9.22$ Hz), 140.9, 145.5 (dd, $J = 12.47/241.35$ Hz), 149.0 (dd, $J = 12.96/242.84$ Hz), 165.9. ESI-MS (m/z): calcd. for $C_{15}H_{11}F_2N_3O$: 287.087; found 286.071 $[M - H]^-$, 288.098 $[M + H]^+$.

5.1.2.6. *N*-(3,4-difluorophenyl)-2-methyl-2*H*-indazole-5-carboxamide (**14b**)

Purification according to RP-HPLC method 3 yielded **14b** as a white solid (12 mg, 18%); mp 187.8–188.1°C. 1H NMR (500 MHz, DMSO- d_6) $\delta = 4.21$ (s, 3H, N2Me), 7.41 (qd, $J = 10.4/10.72$ Hz, 1H, Ph), 7.54–7.59 (m, 1H, Ph), 7.68 (dt, $J = 9.14/0.95$ Hz, 1H, Ph), 7.77 (dd, $J = 1.57/9.14$ Hz, 1H, Ph), 7.95 (ddd, $J = 2.53/7.57/13.25$ Hz, 1H, Ph), 8.43 (q, $J = 0.63$ Hz, 1H), 8.59 (s, 1H, ind-het), 10.39 (s, 1H, -CONH-). ^{13}C NMR (125 MHz, DMSO- d_6) $\delta = 39.2$ (N2Me), 109.2 (d, $J = 21.7$ Hz), 116.6 (q, $J = 3.24$ Hz), 116.8, 117.4 (d, $J = 17.7$ Hz), 120.9, 122.1, 124.5, 127.0, 127.2, 136.7 (dd, $J = 2.74/9.22$ Hz), 145.5 (dd, $J = 12.46/241.59$ Hz), 149.0, 149.0 (dd, $J = 13.21/242.84$ Hz), 166.2. ESI-MS (m/z): calcd. for $C_{15}H_{11}F_2N_3O$: 287.087; found 286.021 ($[M - H]^-$), 288.098 $[M + H]^+$.

5.1.3. Preparation of *N*-(3,4-dichlorophenyl)-1-(2-methoxyethyl)-1*H*-indazole-5-carboxamide (**15**)

A solution of 1-(2-methoxyethyl)-1*H*-indazole-5-carboxylic acid (**7**, 97.8 mg, 0.44 mmol), 3,4-dichloroaniline (**3**, 71.3 mg, 0.44 mmol), EDC-HCl (90.0 mg, 0.47 mmol), DIPEA (39.0 μ L, 0.23

mmol) in DMF (5 mL) was stirred over night at room temperature under nitrogen. The reaction was concentrated in vacuo, the residual was treated with a water/ether mixture (4:1, 50 mL), and the mixture was stirred for 30 min at room temperature. The precipitate formed was filtered under reduced pressure, washed three times with water (10 mL), and dried at 70 °C. The crude product was purified by column chromatography on silica gel (mobile phase: CH₂Cl₂/MeOH 9/1 v/v) following by recrystallization from methanol to yield **15** as colorless crystals (82 mg, 51%); mp 116.8–117.8°C. ¹H NMR (500 MHz, DMSO-*d*₆) δ = 3.18 (s, 3H, OMe), 3.77 (t, *J* = 5.36 Hz, 2H, CH₂), 4.61 (t, *J* = 5.04 Hz, 2H, NCH₂), 7.60 (d, *J* = 8.82 Hz, 1H, Ph), 7.78 (dd, *J* = 2.21/8.83 Hz, 1H, Ph), 7.79 (d, *J* = 8.83 Hz, 1H, Ph), 7.95 (dd, *J* = 1.58/8.83 Hz, 1H, Ph), 8.18 (d, *J* = 2.21 Hz, 1H, Ph), 8.28 (s, 1H, ind-het), 8.46 (s, 1H, Ph), 10.46 (s, 1H, -CONH-). ¹³C NMR (125 MHz, DMSO-*d*₆) δ = 48.4, 58.2, 70.7, 110.1, 120.3, 121.5, 121.8, 123.0, 125.0, 125.6, 126.8, 130.6, 131.0, 134.6, 139.7, 141.2, 166.1. ESI-MS (*m/z*): calcd. for C₁₇H₁₅Cl₂N₃O₂: 363.054; found 362.281 [M – H][–], 364.112 [M + H]⁺.

5.1.4. Modified procedure for the preparation of N1-/N2-methylated indazole mixtures

The respective mixtures of N1-/N2-methylated regioisomers were prepared following the General Procedure for the preparation of *N*-methylated indazoles with small modifications. Briefly, a solution of the corresponding indazole-5-carboxamide (1.0 equiv) and potassium carbonate (1.2 equiv) in DMF was stirred for 1 hour at room temperature and treated with MMS (method 1) or methyl iodide (method 2) (1.2 equiv). The reaction was stirred for an appropriate time before additional amounts of the respective base were added. The mixture was further stirred at room temperature until conversion completed. Aqueous work-up of the reaction was carried out as described above. Re-crystallization from methanol afforded a mixture of pure N1-/N2-regioisomers (>97% by LC/ESI-MS analysis) as white solids with an overage yield of more than 80%.

5.1.5. General procedure for the preparation of hydrochlorides

The respective hydrochlorides were prepared by treating the compounds with 4.0 M hydrogen hydrochloride solution in dioxane and subsequent stirring for an appropriate time at room temperature. The yellowish precipitate formed was filtered under reduced pressure, washed with ether and dried for several days at 70 °C.

5.1.6. General procedure for the preparation of triflates

The triflates were prepared by dissolving the compounds in a minimum quantity of neat trifluoroacetic acid (TFA) and subsequent stirring for an appropriate time at room temperature. The excess of acid was evaporated and the traces of TFA were removed by co-evaporation with toluene. The yellowish solid was washed with petroleum ether, filtered and dried at 70 °C.

5.2. Monoamine oxidase inhibition assays

Assays of monoamine oxidase inhibitory activities of compounds in Table 1 were performed as previously described [30,31] using a continuous fluorescence-based method [35,36]. Test samples for the MAO assays (1.0% final concentration in DMSO) were prepared as reported earlier [30]. The following stock solutions were used: test compounds (10 mM) in DMSO, reference MAO inhibitors (0.5 mM), *p*-tyramine (100 mM), and resorufin sodium salt (2.0 mM) in deionized water. MAO inhibition was determined using commercially available recombinant human MAO-A and MAO-B enzymes expressed in baculovirus-infected BTI insect cells (Sigma-Aldrich, M7316 and M7441) and enzyme-containing mitochondrial-enriched fractions of rat, obtained from livers of male Sprague-Dawley rats [31]. Rat liver mitochondria were pretreated for 15 min at RT with an aqueous solution of the irreversible inhibitors clorgyline (30 nM) or selegiline (300 nM) to block the respective MAO-A or MAO-B activity. *p*-tyramine was used as a substrate in a final concentration of 300 μM for the rat and 150 μM for the human MAO assays, respectively. Rat and human MAO inhibition assays were performed in triplicate at RT in 96-well plates (200 μL final volume) using the commercial MAO assay

kit Aplex Red (pH 7.4). Clorgyline for MAO-A and selegiline for MAO-B were used to determine the non-MAO-A and non-MAO-B enzyme activity, respectively. Fluorescent measurements were performed for 45 min and the concentration-response curves of the reference inhibitors clorgyline (MAO-A) and selegiline (MAO-B) served as positive controls for both rat and human MAO assays. In all MAO assays, the reference inhibitors clorgyline and selegiline were used in a final concentration of 1.0 μM . A sample with DMSO (2.0 μL) served as a negative control.

Inhibition of MAO enzymes was measured with at least two initial concentrations (10 and 0.1 μM) followed by determination of full inhibition curves of the respective active compound. IC_{50} values were determined by nonlinear regression analysis of MAO inhibition versus the logarithm (-log) of the tested compound molar concentration and calculated by mean IC_{50} value \pm SEM (standard error of the mean) of at least three independent experiments using GraphPad Prism v.4.0 software. K_i values were calculated from mean IC_{50} according to the Cheng-Prusoff equation [49] $K_i = \text{IC}_{50}/(1+[S]/K_m)$, where [S] is the substrate concentration (*p*-tyramine) and K_m its concentration required to reach half-maximal velocity (Michaelis constant, $V_{\text{max}}/2$).

5.3. Crystallography

Crystals for X-ray structure analysis were grown from methanol (1.5–2 mL) for **9**, **12a** and **13a** or methanol–water solution (2:1, 3.0 mL), methanol and acetonitrile for **11** by slowly evaporation of the solvent at room temperature. For compound **11**, single crystals in methanol–water solution were obtained directly from their mother liqueur containing minimum water (0.2–0.3 mL). The crystal data were collected on a Rigaku Oxford Diffraction diffractometer with Atlas detector using Cu K_α radiation. The crystals were kept at 100.0 K during data collection. The structures were solved and refined with the ShelX [66] program package using direct methods and least-squares minimization. All non-hydrogen atoms were refined anisotropically. Hydrogen atoms bound to nitrogen and all hydrogen atoms in **9** were refined isotropically, other hydrogen atoms were placed in calculated positions and refined using a riding model. For molecular graphics Olex2 [67] and Ortep [68] programs were used.

The crystallographic data and refinement results of all structures are given in the Supporting information.

CCDC 1501429 (**9**), CCDC 1501430 (**11**), CCDC 1501431 (**12a**), and CCDC 1501432 (**13a**) contain the supplementary crystallographic data for this paper. These data can be obtained free of charge from The Cambridge Crystallographic Data Centre via www.ccdc.cam.ac.uk/data_request/cif.

5.4. Molecular modeling studies

5.4.1. Ligand and protein preparation, ligand ADME

Ligand input structures were taken from the respective small molecule crystal X-ray structures and used without any further manual preparation. In fact, it turned out that the X-ray crystallographically determined bond lengths and angles for **9**, **11**, **12a** and **13a** led to an excellent predictivity for experiment – in contrast to coordinates generated by the MMFF94x force-field. The crystal structures of the human MAO-A in complex with harmine (PDB code: 2Z5X) [40] and the human MAO-B in complex with safinamide (PDB code: 2V5Z) [41] were retrieved from the Protein Databank (PDB). For the docking experiments with the human MAO-B co-crystal structure, all computations were performed in the 2V5Z chain B; the ProToss routines in SeeSAR protonate accordingly (cp. below) and select the most energetically favored tautomer in the framework of its model (for details, see Supporting Information). Ligand ADME estimations were carried out using the StarDrop model runner algorithms in SeeSAR v.5.4 [43].

5.4.2. Pose generation and docking

For dockings, unless otherwise mentioned, we used FlexX docking module in LeadIT v.2.1.8 from BioSolveIT with the same procedure as documented earlier (see Supporting Information) [30]. The docking algorithm in LeadIT relies on the FlexX and SIS incremental build-ups schemes [69,70]. LeadIT has both accurately reproduced the experimental harmine and safinamide binding modes on high ranks and proven to yield very plausible and well-scored poses of the active compounds discussed

in this and earlier works. The selected poses share a large part of the harmine and safinamide pocket from the corresponding PDB structures. In some cases the SeeSAR-integrated docking engine was applied. This algorithm is similar to the FlexX/-SIS algorithms described above, but differs in details of the torsional sampling. In SeeSAR, a maximum of 10 poses is output.

5.4.3. HYDE scoring and visualization

5.4.3.1. Entropic and enthalpic terms

Once generated, the top 32 LeadIT poses were filed into SeeSAR (cf. below) for post-scoring with HYDE [42]. The latest HYDE implementation is integrated in SeeSAR v.5.4 from BioSolveIT [43]. SeeSAR visualizes the estimated free energy of binding in the framework of the HYDE atomic logP increment model using "coronas" that range from large dark red (very unfavorable) to large dark green spheres (very favorable for affinity) [71]. The estimations of the Free Energy of binding are computed within a few seconds, the software enables quick and interactive assessments of energies and torsions (cp. below). The algorithm that proposes protonation/tautomers and that selects and orients the water molecules is called Protoss and was recently published [72]. HYDE determines the desolvation (or more appropriately, the dehydration) and enthalpic contributions to binding based on an untrained physical model. Since the equations are based on atomic increments, SeeSAR can visualize and quantitatively report both protein and ligand contributions. It further allows a (semi-)quantitative estimation of the thermodynamic profile by adding up the atom-wise enthalpic (hydrogen bridges/salt bridges) and entropic (desolvation) parts in the HYDE equations, respectively.

5.4.3.2. Clash and torsion

Because clash and torsional strain are not integrated in the HYDE mathematical kernel, there is a pre-optimization involved that is limited (capped) to small movements only ensuring the binding mode remains as determined by the user. We selected poses based on their visual HYDE scores and on a torsional analysis, as published [73,74]. In addition, we used the visualization of the "tightness of fit"

(grey, cloud-like shaped "fog" signifying room for at least one fluorine atom between ligand and protein) to guide decisions when insecure CSD-based statistical analyses for torsions and their frequency of occurrence in the Cambridge small molecule crystal structure database (CSD) are encoded as a traffic-light visualization is in SeeSAR (from green = often observed to red = rarely or never seen) [74]. For more details regarding docking experiments, HYDE analysis and its implementation for rational-HYDE-based drug design, see the Supporting information including the project files (*.seesar). The project files can be obtained with freely downloadable SeeSAR packages [43].

5.5. ADME studies

5.5.1. Determination of kinetic solubility

Chemicals for preparing of phosphate buffer were purchased from Sigma-Aldrich. KOH (Chempur) and acetonitrile (J.T. Baker) were of *pro analysis* grade. The investigated compounds (10 μ L stock solution in DMSO) were diluted with 0.06 M phosphate buffer (190 μ L) at the corresponding pH value (2.0, 5.5 and 7.4) to a final concentration of 500 μ M (5.0% DMSO). Assays were performed at RT. Prior using, the pH of each buffer system was adjusted to the appropriate target value. The working solutions (200 μ L) of tested compounds were dispensed into a 96-well filter plate (Millipore) and incubated for 90 minutes while shaking at 500 rpm on a MTP thermomixer Comfort 5355 (Eppendorf). After that time, the filter plate was placed inside the vacuum manifold (Waters) and filtered. After filtration, 100 μ L of samples were collected, transferred onto a UV-Vis transparent 96-well analysis plate (Eppendorf), and acetonitrile (100 μ L) was added to each well to a final volume of 200 μ L. The concentration of the compounds was determined on the basis of the corresponding calibration curves using UV-Vis spectrophotometric method. Calibration curves were prepared by serial dilution of 500 μ M solution of compounds (two series of seven 1:1 dilutions) with acetonitrile and addition of 100 μ L of 60 mM phosphate buffer (pH 2.0, 5.5, and 7.4) to a final volume of 200 μ L. The concentrations used for calibration were 3.91, 7.81, 15.63, 31.25, 62.5, 125, 250 and 500 μ M. Increased UV absorbance of tested compounds was measured on a Synergy 2 multi-detection microplate reader (BioTech) across the

range of 250–500 nm. For each compound, the maximum absorbance (λ_{max}) was chosen in order to determine concentration. The equations resulting from the calibration curves were used for calculating the concentration. The solubility at pH 2.0, 5.5, and 7.4 was the mean \pm SD of three independent assays.

5.5.2. Determination of *LogD*

The octanol-water distribution coefficient (*LogD*) of investigated and reference compounds was determined by shake-flask method using an aqueous media of 60 mM phosphate buffer at pH 2.0, 5.5, and 7.4. Assays were performed in UV compatible 96-well analysis plates (Eppendorf) at RT. *n*-Octanol (Sigma-Aldrich) and buffer (pH 2.0, 5.5, and 7.4) were saturated for 24 hours on a mechanical shaker (JWElectronic). After shaking, the mixture was left untouched for another 24 hours allowing the layers to separate and achieve a saturation state. A 1782 μL of 0.06 M phosphate solution saturated with *n*-octanol and 18 μL of the tested compound (10 mM in DMSO, initial concentration 100 μM) were successively added to Eppendorf tubes. Then, 200 μL of *n*-octanol saturated with 60 mM phosphate buffer (pH 2.0, 5.5, and 7.4) was added to a final volume of 2000 μL and the tubes were shaken for 90 min at 900 rpm on MTP thermomixer Comfort 5355 (Eppendorf). After shaking, the tubes were left for two hours in order to allow separation of both phases. Then, samples (100 μL) from each phase were collected and transferred into a 96-well analysis plate and measured using UV-Vis spectrophotometry. The concentration of each compound was determined on the basis of calibration curves for both phases buffer (for pH 2.2, 5.5, and 7.4) and *n*-octanol. Calibration curves were prepared in duplicates by serial dilution of 100 μM (for buffer, 9 concentrations) and 400 μM (for *n*-octanol, 8 concentrations) solution of compounds (two series of seven 1:1 dilutions) with buffer or *n*-octanol, respectively. Stock solutions in DMSO (10 mM) of the commercially available (Sigma-Aldrich) Ketoconazole (MW 531.43 g/mol) and Metoprolol (MW 684.81 g/mol) were used as references for lipophilic and hydrophilic compounds, respectively. UV measurements of tested and reference compounds were performed as described above. The equations resulting from the calibration curves were used for calculation of compounds

concentration in both aqueous and *n*-octanol layers. The LogD was calculated at pH 2.0, 5.5, and 7.4 according to the following equation:

$$\text{Log}D_{pH(x)} = \log\left(\frac{C_{oct.}}{C_{buffer\ pH(x)}}\right) \quad (1)$$

where $D_{pH(x)}$ is the distribution coefficient, $C_{oct.}$ and $C_{buffer\ pH(x)}$ are the concentration of compound in *n*-octanol and buffer phase at the corresponding pH value, respectively. The LogD values reported correspond to the mean \pm SD of three independent assays.

5.5.3. Determination of PAMPA-GI permeability

Commercial drugs, *n*-dodecane and L- α -phosphatidylcholine were purchased from Sigma-Aldrich. Ethanol (J.T. Baker) was of *pro analysis* grade and used without further purification. The donor 96-well filter plate (MultiScreen, PVDF membrane, pore size 45 μm), the acceptor 96-well plate (MultiScreen, PTFE membrane), and the 96-well MultiScreen transport receiver plate were obtained from Millipore. Assays were performed at RT without stirring. Investigated and reference compounds were diluted with 60 mM phosphate buffer (at pH 2.0, 5.5, and 7.4) and ethanol (20%) to a final concentration of 200, 100 or 50 μM by mixing 980, 990 or 995 μL buffers with 20, 10 or 5 μL , respectively, of 10 mM stock solution in DMSO for each compound. The final concentration of DMSO in the corresponding working solution was chosen based on the kinetic solubility results for each compound and was equal to 2, 1 or 0.5%, respectively. A lipid solution of L- α -phosphatidylcholine (1%) was prepared by dissolving a weighted amount of compound in an appropriate volume of *n*-dodecane. The filter membrane in the donor microplate was pre-coated with 5.0 μL of lipid solution. Then, 150 μL of working solution of tested and reference compounds were dispensed into the corresponding wells of the donor plate, while 300 μL of phosphate buffer (pH 7.4)/20% ethanol/DMSO were added to the appropriate wells of the acceptor plate. The donor plate was inserted into the receiver plate and the sandwich assembly was incubated for 4 hours while shaking at 500 rpm. After incubation time, 100 μL of samples from both donor and acceptor compartments were collected and transferred into a UV compatible 96-well analysis

plate (Eppendorf) for UV-Vis measurement. Calibration curves were prepared in duplicates by serial dilution of 100 μ M solution of investigated and reference compounds by adding of a mixture of 100 μ L phosphate buffer (60 mM, pH 7.4) with 20% ethanol and DMSO (0.5%) for both donor and acceptor compartments. Commercially available verapamil (MW 454.60 g/mol) and theophylline (MW 180.16 g/mol) were used as references for compounds of high and low permeability, respectively. UV absorbance of tested and reference compounds were measured using UV-Vis spectrophotometry. The equations resulting from the calibration curves were used for calculating compounds concentrations in both donor and acceptor compartments after incubation time. The *effective* permeability coefficient (P_e) measured for gastrointestinal conditions was calculated at pH 2.0, 5.5, and 7.4 according to the following equation:

$$P_e = C - \ln\left(1 - \frac{C_a}{C_r}\right) \quad (2)$$

where

$$C = \frac{V_d V_a}{(V_d + V_a) p t} \quad (3)$$

The mass balance (MB) parameter was calculated based on the following equation:

$$MB(\%) = \frac{(C_a V_a) + (C_d V_d)}{C_{initial} V_d} \times 100 \quad (4)$$

where V_a and V_d are the volumes of acceptor and donor compartment, C_a and C_d are the concentrations in acceptor and donor compartments after incubation, $C_{initial}$ and C_r are initial concentration in donor and concentration in equilibrium, p is membrane surface area (0.28 cm^2), and t is the time (s). The P_e values reported correspond to the mean \pm SD of three independent assays.

5.5.4. Determination of PAMPA-BBB penetration

PAMPA permeability across artificial BBB lipid membrane was determined in 60 mM phosphate buffer (pH 7.4), as described above for PAMPA-GI with the exception of the respective lipid composition used. The artificial biological membrane was constructed by coating the porous membrane of a donor

96-well filter plate with 1.0% solution of porcine polar brain lipid (PBL) extract. Briefly, the investigated and reference compounds were precisely dissolved in an appropriate volume of *n*-dodecane and dispensed into the donor plate, while the buffer was placed into the acceptor chamber. The device was incubated for 4 hours at RT and shaken to ensure good solvent mixing and a decrease of unstirred water layer on the artificial membrane surface. After incubation, the samples were collected and the concentrations of investigated and reference compounds were determined in both donor and acceptor plates using UV-Vis spectrophotometry. Based on prepared calibration curves and measured UV absorbance at compounds specific λ_{max} , concentrations in both of compartments were calculated (for details, see Supporting Information). The *effective* permeability coefficient (P_e) and mass balance (MB) measured under BBB conditions were calculated according to equations 2–4. The P_e values reported correspond to the mean \pm SD of three independent assays.

Acknowledgments

The authors would like to thank Dr. Sonja Hinz and Dr. Petra Küppers for providing the initial results of pharmacological assays. N.T.T. thanks Angelika Fischer and Anika Püsche for technical assistance in performing initial MAO assays, Marion Schneider for performing LC/MS analyses, and Sabine Terhart-Krabbe and Anette Reiner for recording NMR spectra. L.A. and S.H. thank the Swiss National Science Foundation (Tautocrown Joint research project and SupraMedChem@Balkans.Net Institutional partnership project under SCOPES Program), Alexander von Humboldt Foundation (equipment donation) and Bulgarian Science Fund (access to MADARA computer cluster by project RNF01/0110) for the generous support. M.G. thanks Dr. Matthew Segall and Nicholas Foster from Optibrium, UK, for a license to use the new StarDrop ADME module in SeeSAR v.5.4 for this work.

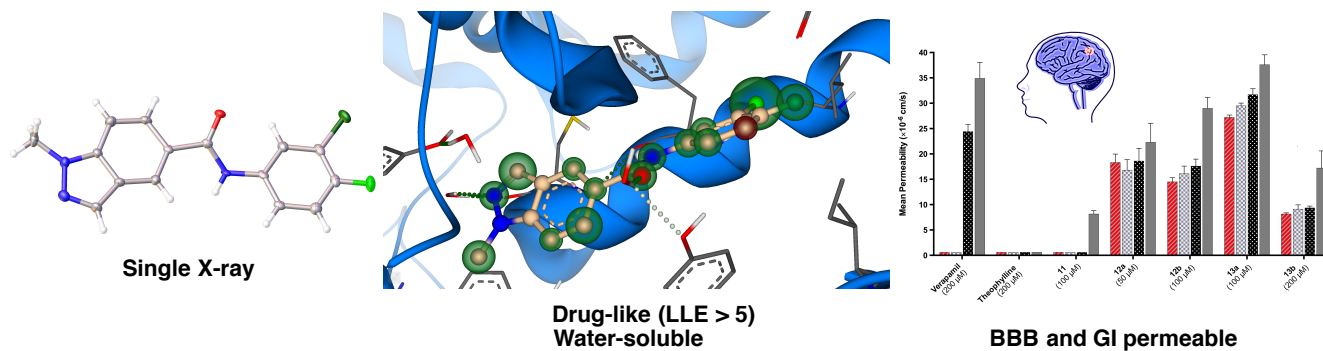
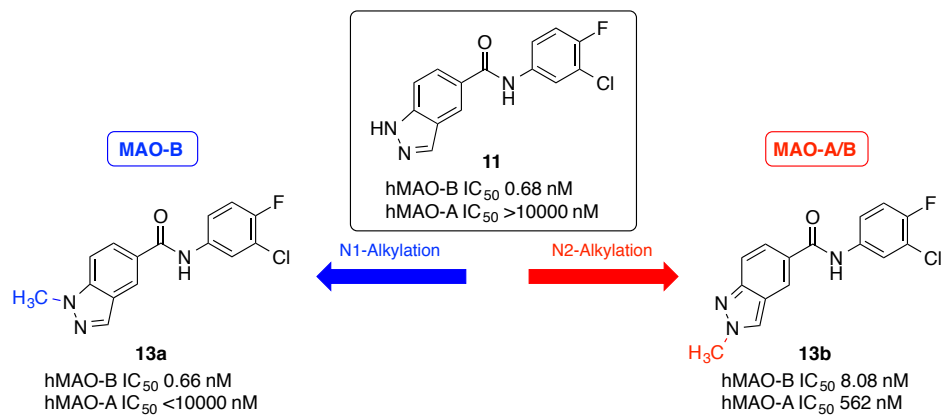
Appendix A. Supplementary data

Supplementary data related to this article can be found at <http://dx.doi.org/...>

ABBREVIATIONS USED

ACN, acetonitrile; AD, Alzheimer's disease; BEI, binding efficiency index; BBB, blood-brain barrier; CHO, Chinese hamster ovary; CNS, central nervous system; COMT, catechol-*O*-methyltransferase; DA, dopamine; DIPEA, *N,N*-diisopropylethylamine; DMF, *N,N*-dimethylformamide; DMSO, dimethylsulfoxide; DDIs, DOPA-decarboxylase inhibitors; EDC, 1-ethyl-3-(3-dimethylaminopropyl)-carbodiimide; EGTA, ethyleneglycoltetraacetic acid; ESI, electrospray ionization; FAD, flavin adenine dinucleotide; GIT, gastrointestinal tract; h, human; HA, heavy atom; HBD, hydrogen bonding domain; HBS, halogen binding subpocket; HIA, human intestinal absorption; HMBC, heteronuclear multiple bond correlation; HRP, horseradish peroxidase; HYDE, hydrogen dehydration; LE, ligand efficiency; LLE, lipophilic ligand efficiency; MAO, monoamine oxidase; MMS, methyl methanesulfonate; PAMPA, parallel artificial membrane permeability; PBL, polar brain lipid; PD, Parkinson's disease; PNS, peripheral nervous system; PET, positron emission tomography; r, rat; ROS, reactive oxygen species; SAR, structure-activity relationship; SSR, structure-selectivity relationship; TLC, thin-layer chromatography.

TABLE OF CONTENTS GRAPHIC



Highlights

- Selective MAO-B and dual MAO-A/B inhibitors have been developed.
- *N*-methylated indazole-5-carboxamides show high GI and BBB *in vitro* permeability, **13a** and **13b** exhibiting also excellent drug-like properties.
- Visual SAR guidance with new modeling techniques successfully applied.
- Comprehensive binding mode and pharmacophore feature analyses conducted.

References

- [1] A.K. Kakkar, N. Dahiya, Management of Parkinson's disease: Current and future pharmacology, *Eur. J. Pharmacol.* 750 (2015) 74–81.
- [2] A. Samii, J.G. Nutt, B.R. Ransom, Parkinson's disease, *Lancet* 363 (2004) 1783–1793.
- [3] C. Singer, Managing the patient with newly diagnosed Parkinson's disease, *Clev. Clin. J. Med.* 79 (Suppl. 2) (2012) S3–S7.
- [4] J.M. Zigmond, R.J. Smeyne, Exercise: Is it a neuroprotective and if so, how does it work?, *Parkinsonism Rel. Disord.* 20 (Suppl. 1) (2014) S123–S127.
- [5] W. Dauer, S. Przedborski, Parkinson's disease: Mechanism and models, *Neuron* 39 (2003) 889–909.
- [6] J.-A. Girault, P. Greengard, The neurobiology of dopamine signaling, *Arch. Neurol.* 61 (2004) 641–644.
- [7] Y. Imai, B. Lu, Mitochondrial dynamics and mitophagy in Parkinson's disease: Disordered cellular power plant becomes a big deal in a major movement disorder, *Curr. Opin. Neurobiol.* 21 (2011) 935–941.
- [8] T. Kondo, Y. Mizuno, Japanese Istradefylline Study Group, A long-term study of istradefylline safety and efficacy in patients with Parkinson's disease, *Clin. Neuropharmacol.* 38 (2015) 41–46.
- [9] P. Dunkel, C.L. Chai, B. Sperlágh, P.B. Huleatt, P. Mátyus, Clinical utility of neuroprotective agents in neurodegenerative disease: current status of drug development for Alzheimer's, Parkinson's and Huntington's diseases, and amyotrophic lateral sclerosis, *Exp. Opin. Investig. Drugs* 21 (2012) 1267–1308.
- [10] J. Jankovic, W. Poewe, Therapies in Parkinson's disease, *Curr. Opin. Neurol.* 25 (2012) 433–447.

- [11] J.H. Kurth, M.C. Kurth, Role of monoamine oxidase genetics in the etiology of Parkinson's disease, In: A. Lieberman, C.W. Olanow, M.B.H. Youdim, K. Tipton (Eds.), *Monoamine Oxidase Inhibitors in Neurological Diseases*, Marcel Dekker Inc., New York, 1994, pp. 113–126.
- [12] A. Whibley, J. Urquhart, J. Dore, L. Willatt, G. Parkin, L. Gaunt, G. Black, D. Donnai, F.L. Raymond, Deletion of MAOA and MAOB in a male patient causes severe developmental delay, intermittent hypotonia and stereotypical hand movements, *Eur. J. Hum. Gen.* 18 (2010) 1095–1099.
- [13] J. Tong, J.H. Meyer, Y. Furukawa, L. Boileau, L.-J. Chang, A.A. Wilson, S. Houle, S.J. Kish, Distribution of monoamine oxidase proteins in human brain: Implication for brain imaging studies, *J. Cereb. Blood Flow Metab.* 33 (2013) 863–871.
- [14] J.C. Shih, K. Chen, M.J. Ridd, Monoamine oxidase: From genes to behavior, *Ann. Rev. Neurosci.* 22 (1999) 197–217.
- [15] A. Nicotra, F. Pierucci, H. Parvez, O. Senatori, Monoamine oxidase expression during development and aging, *NeuroToxicology* 25 (2004) 155–165.
- [16] M.B.H. Youdim, L. Lavie, Selective MAO-A and MAO-B inhibitors, radical scavengers and nitric oxide synthase inhibitors in Parkinson's disease, *Life Sci.* 55 (1994) 2077–2082.
- [17] B.P. Kennedy, M.G. Ziegler, M. Alford, L.A. Hansen, L.J. Thal, E. Masliah, Early and persistent alterations in prefrontal cortex MAO A and B in Alzheimer's disease, *J. Neural Transm.* 110 (2003) 789–801.
- [18] L. Emilsson, P. Saetre, J. Balciuniene, A. Castensson, N. Cairns, E.E. Jazin, Increased monoamine oxidase messenger RNA expression levels in frontal cortex of Alzheimer's disease patients, *Neurosci. Lett.* 326 (2002) 56–60.
- [19] P. Riederer, L. Lachenmayer, G. Laux, Clinical applications of MAO-inhibitors, *Curr. Med. Chem.* 11 (2004) 2033–2043.

- [20] F. Lotufo-Neto, M. Trivedi, M.E. Thase, Meta-analysis of the reversible inhibitors of monoamine oxidase type A moclobemide and brofaromine for the treatment of depression, *Neuropsychopharmacol.* 20 (1999) 226–247.
- [21] J.S. Fowler, J. Logan, N.D. Volkow, E. Shumay, F. McCall-Perez, M. Jayne, G.-J. Wang, D.L. Alexoff, K. Apelskog-Torres, B. Hubbard, P. Carter, P. King, S. Fahn, M. Gilmore, F. Telang, C. Shea, Y. Xu, L. Muench, Evidence that formulations of the selective MAO-B inhibitor selegiline, which bypass first-pass metabolism, also inhibit MAO-A in the human brain, *Neuropsychopharmacol.* 40 (2015) 650–657.
- [22] S.E. Lakhan, From a Parkinson's disease expert: Rasagiline and the future of therapy, *Mol. Neurodegener.* 2 (2007) 1–3.
- [23] B. Kumar, Sheetal, A.K. Mantha, V. Kumar, Recent developments on the structure-activity relationship studies of MAO inhibitors and their role in different neurological disorders, *RSC Adv.* 6 (2016) 42660–42683.
- [24] E.D. Deeks, Safinamide: first global approval, *Drugs* 75 (2015) 705–711.
- [25] C. Cattaneo, R. La Ferla, E. Bonizzoni, M. Sardina, Long-term effects of safinamide on dyskinesia in mid-to late-stage Parkinson's disease: A post-hoc analysis, *J. Parkinson's Dis.* 5 (2015) 475–481.
- [26] M. Fabbri, M.M. Rosa, D. Abreu, J.J. Ferreira, Clinical pharmacology review of safinamide for the treatment of Parkinson's disease, *Neurodegener. Dis. Manag.* 5 (2015) 481–496.
- [27] S. Carradori, R. Silvestri, New frontiers in selective human MAO-B inhibitors, *J. Med. Chem.* 58 (2015) 6717–6732.
- [28] J.J. Joubert, J.P. Petzer, L.H.A. Prins, B.P. Repsold, S.F. Malan, Multifunctional enzyme inhibition for neuroprotection – A focus on MAO, NOS, and AChE inhibitors, In: Atta-ur-Rahman, M.I. Choudhary (Eds.), *Drug Design and Discovery in Alzheimer's Disease*, Elsevier Science Publishing Company Inc., Amsterdam, 2015, pp. 291–365.

- [29] M.B.H. Youdim, L. Kupersmidt, T. Amit, O. Weinreb, Promises of novel multi-target neuroprotective and neurorestorative drugs for Parkinson's disease, *Parkinsonism Relat. Disord.* 20S1 (2014) S132–S136.
- [30] N.T. Tzvetkov, S. Hinz, P. Küppers, M. Gastreich, C.E. Müller, Indazole- and Indole-5-carboxamides: Selective and reversible monoamine oxidase B inhibitors with subnanomolar potency, *J. Med. Chem.* 57 (2014) 6679–6703.
- [31] N.T. Tzvetkov, Substituted indazole or indole derivatives as in vitro MAO-B inhibitors, 2014, WO2014/107771.
- [32] M. Gastreich, N.T. Tzvetkov, Visual rationalizing of activity against Parkinson's and Alzheimer's disease: Reversible MAO-B Inhibitors with subnanomolar potency, FMC, Antwerp, Belgium, September 14-16, 2015, P026.
- [33] L.H.A. Prins, J.P. Petzer, S.F. Malan, Inhibition of monoamine oxidase by indole and benzofuran derivatives, *Eur. J. Med. Chem.* 45 (2010) 4458–4466.
- [34] N.T. Tzvetkov, B. Neumann, H.-G. Stammler, L. Antonov A simple approach to multifunctionalized N1-alkylated 7-amino-6-azaoxindole derivatives using there in situ stabilized tautomer form, *Tetrahedron* 72 (2016) 6455–6466.
- [35] A. Holt, D.F. Sharman, G.B. Baker, M.M. Palcie, A continuous spectrophotometric assay for monoamine oxidase and related enzymes in tissue homogenates, *Anal. Biochem.* 244 (1997) 384–392.
- [36] J.G. Mohanty, J.S. Jaffe, E.S. Schulman, D.G. Raible, A highly sensitive fluorescent micro-assay of H₂O₂ release from activated human leukocytes using a dihydroxyphenoxazine derivative, *J. Immunol. Methods* 202 (1997) 133–141.
- [37] M.J. Matos, F. Rodríguez-Enrí, S. Vilar, L. Santana, E. Uriarte, G. Hripcsak, M. Estrada, M.I. Rodríguez-Franco, D. Viña, Potent and selective MAO-B inhibitors activity: Amino- versus nitro-3-arylcoumarin derivatives, *Bioorg. Med. Chem. Lett.* 25 (2015) 642–648.

- [38] C. Binda, F. Hubálek, L. Min, Y. Herzig, J. Sterling, P. Salvati, D.E. Edmondson, A. Mattevi, A crystal structure of monoamine oxidase B in complex with four inhibitors of the N-propargylaminoindan class, *J. Med. Chem.* 47 (2004) 1767–1774.
- [39] N.T. Tzvetkov, I.K. Pajeva, Binding and interactions of a novel potent indole-5-carboxamide MAO-B inhibitor, *Compt. Rend. Acad. Bulg. Sci.* 67 (2014) 937–942.
- [40] S.Y. Son, J. Ma, Y. Kondou, M. Yoshimura, E. Yamashita, T. Tsukihara, Structure of human monoamine oxidase A at 2.2 Å resolution: The control of opening the entry for substrates/inhibitors, *Proc. Natl. Acad. Sci. U.S.A.* 105 (2008) 5739–5744.
- [41] C. Binda, J. Wang, L. Pisani, C. Caccia, A. Carotti, P. Salvati, D.E. Edmondson, A. Mattevi, Structures of monoamine oxidase B complexes with selective non-covalent inhibitors: safinamide and coumarin analogs, *J. Med. Chem.* 50 (2007) 5848–5852.
- [42] LeadIT v.2.1.9, BioSolveIT GmbH, Sankt Augustin, Germany, 2016. <http://www.biosolveit.de>.
- [43] SeeSAR v5.4, BioSolveIT GmbH, Sankt Augustin, Germany, 2016. <http://www.biosolveit.de>.
- [44] N. Schneider, G. Lange, S. Hindle, R. Klein, M. Rarey, A consistent description of HYdrogen bond and DEhydration energies in protein-ligand complexes: Methods behind the HYDE scoring function, *J. Comput.-Aided Mol. Des.* 27 (2013) 15–29.
- [45] These docking pose graphics were generated with the UCSF Chimera package v.1.10.2. Chimera is developed by the Resource for Biocomputing, Visualization, and Informatics at the University of California, San Francisco (supported by NIGMS P41-GM103311).
- [46] F.X. Ruiz, A. Cousido-Siah, S. Porté, M. Dominguez, I. Crespo, C. Rechlin, A. Mitschler, A.R. de Lera, M.J. Martín, J.À. de la Fuente, G. Klebe, X. Parés, J. Farrés, A. Podjarny, Structural determination of the selectivity of 3-benzyluracil-1-acetic acids towards human enzymes aldose reductase and AKR1B10, *ChemMedChem* 10 (2015) 1989–2003.
- [47] G. Klebe, Applying thermodynamic profiling in lead finding and optimization, *Nature Rev. Drug Discov.* 14 (2015) 95–110.

- [48] M. Betz, T. Wulsdorf, S.G. Krimmer, G. Klebe, Impact of surface water layers on protein–ligand binding: How well are experimental data reproduced by molecular dynamics simulations in a thermilysin test case, *J. Chem. Inf. Model.* 56 (2016) 223–233.
- [49] Y.C. Cheng, W.H. Prusoff, Relationships between the inhibition constant (K_i) and the concentration of inhibitor which causes 50% inhibition (IC_{50}) of an enzymatic reaction, *Biochem. Pharmacol.* 22 (1973) 3099–3108.
- [50] J. Reis, F. Cagide, D. Chavarria, T. Silva, C. Fernandes, A. Gaspar, E. Uriarte, F. Remião, S. Alcaro, F. Ortuso, F. Borges, Discovery of new chemical entities for old targets: Insights on the lead optimization of chromone-based monoamine oxidase B (MAO-B) inhibitors, *J. Med. Chem.* 59 (2016) 5879–5893.
- [51] S. Kawauchi, L. Antonov, Y. Okuno, Prediction of the color of dyes by using time-dependent density functional theory, *Bulg. Chem. Comm.* 46 (2014) 228-237.
- [52] D.E. Clark, Rapid calculation of polar molecular surface area and its application to the prediction of transport phenomena. I. Prediction of intestinal absorption, *J. Pharm. Sci.* 88 (1999) 807–814.
- [53] S. Vilar, M. Chakrabarti, S. Costanzi, Prediction of passive blood-brain partitioning: Straightforward and effective classification models based on in silico derived physicochemical descriptors, *J. Mol. Graphics Model.* 28 (2010) 899–903.
- [54] K.D. Freeman-Cook, Lipophilic efficiency: the most important efficiency metric in medicinal chemistry, *Future Sci.* 5 (2013) 113–115.
- [55] C. Abad-Zapatero, Ligand efficiency indices for effective drug discovery, *Expert Opin. Drug Discovery* 2 (2007) 469–488.
- [56] T.T. Wager, X. Hou, P.R. Verhoest, A. Villalobos, Moving beyond rules: The development of a central nervous system multiparameter optimization (CNS MPO) approach to enhance alignment of drug-like properties, *ACS Chem. Neurosci.* 1 (2010) 435–449.

- [57] S.A. Hitchcock, L.D. Pennington, Structure-brain exposure relationships, *J. Med. Chem.* 49 (2006) 7559–7583.
- [58] T.W. Johnson, K.R. Dress, M. Edwards, Using the Golden Triangle to optimize clearance and oral absorption, *Bioorg. Med. Chem. Lett.* 19 (2009) 5560–5564.
- [59] J. Alsenz, M. Kansy, High throughput solubility measurement in drug discovery and development, *Adv. Drug Deliv. Rev.* 59 (2007) 546–567.
- [60] L. Di, E.H. Kerns, K. Fan, O.J. McConnell, G.T. Carter, High throughput artificial membrane permeability assay for blood-brain barrier, *Eur. J. Med. Chem.* 38 (2003) 223–232.
- [61] A. Avdeef, Permeability – PAMPA, In: A. Avdeef (Ed.), *Absorption and Drug Development. Solubility, Permeability and Charge State*. John Wiley & Sons, Inc., Hoboken, New Jersey, 2012, pp. 319–498.
- [62] A. Bujard, M. Sol, P.-A. Carrupt, S. Martel, Predicting both passive intestinal absorption and the dissociation constant toward albumin using the PAMPA technique, *Eur. J. Pharm. Sci.* 63 (2014) 36–44.
- [63] B. Sinko, T.M. Garrigues, G.T. Balogh, Z.K. Nagy, O. Tsinman, A. Avdeef, K. Takacs-Novak, Skin-PAMPA: a new method for fast prediction of skin penetration, *Eur. J. Pharm. Sci.* 45 (2012) 698–707.
- [64] A. Avdeef, Physicochemical profiling (solubility, permeability and charge state), *Curr. Top. Med. Chem.* 1 (2001), 277–351.
- [65] C.A. Larregieu, L.Z. Benet, Distinguishing between the permeability relationships with absorption and metabolism to improve BCS and BDDCS predictions in early drug discovery, *Mol. Pharm.* 11 (2014) 1335–1344.
- [66] G.M. Sheldrick, A short history of SHELX, *Acta Crystallogr. A* 64 (2008) 112–122.
- [67] O.V. Dolomanov, L.J. Bourhis, R.J. Gildea, J.A.K. Howard, H. Puschmann, OLEX2: A complete structure solution, refinement and analysis program, *J. Appl. Crystallogr.* 42 (2009) 339–341.

- [68] L.J. Farrugia, WinGX and ORTEP for Windows: An update, *J. Appl. Crystallogr.* 45 (2012) 849–854.
- [69] M. Rarey, B. Kramer, T. Lengauer, G. Klebe, A fast flexible docking method using an incremental construction algorithm, *J. Mol. Biol.* 261 (1996) 470–489.
- [70] C. Lemmen, T. Lengauer, G. Klebe, FlexS: A method for fast flexible ligand superposition, *J. Med. Chem.* 41 (1998) 4502–4520.
- [71] N. Schneider, S. Hindle, G. Lange, R. Klein, J. Albrecht, H. Briem, K. Beyer, H. Claußen, M. Gastreich, C. Lemmen, M. Rarey, Substantial improvements in large-scale redocking and screening using the novel HYDE scoring function, *J. Comput.-Aided Mol. Des.* 26 (2012) 701–723.
- [72] S. Bietz, S. Urbaczek, B. Schulz, M. Rarey, Protoss: A holistic approach to predict tautomers and protonation states in protein-ligand complexes, *J. Cheminform.* (2014) 6:12.
- [73] TorsionAnalyzer was developed in collaboration between F. Hoffmann-LaRoche, Switzerland, and the Center for Bioinformatics (ZBH) of the University of Hamburg: <http://www.biosolveit.de/TorsionAnalyzer/>.
- [74] C. Schärfer, T. Schulz-Gasch, H.C. Ehrlich, W. Guba, M. Rarey, M. Stahl, Torsion angle preferences in drug-like chemical space: A comprehensive guide, *J. Med. Chem.* 56 (2013) 2016–2028.